

Multi-source data-based quantitative risk analysis of road networks to slow-moving landslides

D. Peduto^a, G. Nicodemo^{a,*}, D. Luongo^a, L. Borrelli^b, D. Reale^c, S. Ferlisi^a, G. Fornaro^c, G. Gullà^b

^a Department of Civil Engineering, University of Salerno, Via Giovanni Paolo II, 132, 84084 Fisciano, SA, Italy

^b Research Institute for Geo-Hydrological Protection (IRPI – CNR), National Research Council of Italy, Via Cavour n. 4/6, 87030 Cosenza, Italy

^c Institute for Electromagnetic Sensing of the Environment (IREA – CNR), National Research Council of Italy, Via Diocleziano 328, 80124 Naples, Italy

ARTICLE INFO

Keywords:
Slow-moving landslides
Risk
Roads
Monitoring
Damage
Weathered rocks

ABSTRACT

The paper addresses the quantitative risk analysis for a state road crossing an area of southern Italian Apennines diffusively affected by slow-moving landslides. In this area, Palaeozoic gneissic rocks suffering from intense weathering processes, which produce complex and deep weathering profiles, are present, and this determines severe predisposing conditions to deep-seated slow-moving landslides. Although not directly threatening human lives, for years these slope instabilities have been causing damage and temporary traffic interruptions or limitations to many road sections. To pursue a sustainable landslide risk management, a method that fully exploits multi-disciplinary data consisting of geological-geomorphological features, geotechnical characterization of geomaterials, both conventional (i.e. GPS and inclinometer) and remote sensing (i.e. MT-DInSAR) displacement measurements, in-situ and virtual (i.e. Google Street View images) surveys, and probabilistic tools (i.e. fragility and vulnerability curves) is implemented. As a novelty, such a rich dataset allows overcoming some limitations of the (few) previous studies in the scientific literature on the analysis of the risk posed by slow-moving landslides to roads by exploiting *i*) the multi-temporal recording of the road damage to catch the response of the infrastructure (i.e. both the road pavement and the side retaining structures) with time, and *ii*) the association of the cumulative landslide-induced displacements with the corresponding damage in order to feed empirical forecasting tools for consequence analyses. The thorough knowledge of the slow-moving landslides and their interaction with the exposed roads are implemented within the proposed method to assess the direct economic losses in terms of repair costs, should no countermeasures or mitigation works be implemented in due time. Considering that the studied area resembles very typical conditions of inner roads in hilly and mountain areas of southern Italy, the method can represent a valuable tool for decision makers to prioritize money allocation for risk adaptation and mitigation actions for roads in similar geo-environmental contexts.

1. Introduction

Slow-moving landslides occur in many geo-environmental contexts all over the world threatening the built environment such as structures and infrastructure networks. In Italy, with reference to the main road network, 6180 critical road stretches (i.e. affected by existing landslides) were detected along the highways, state, regional and provincial roads; particularly, 720 of these stretches are along the highways (Trigila et al., 2015). In this country, rich information exists on landslides, their physical characteristics and consequences, whereas much less is known

on their economic impact (Donnini et al., 2017). For instance, the territory of Calabria region (southern Italy) resembles an on-site laboratory in which the effects of slow-moving landslides are recorded on both structures and road assets, with different levels of damage severity depending on the evolutionary stage of the landslide (both single and complex phenomena), the characteristics and typology of the road, and the state of maintenance. An example is provided by the landslide occurred in 2010 in Maierato (Vibo Valentia province, Calabria) which caused the destruction of a road stretch of about 800 m (Borrelli et al., 2014a). Overall, in the region the landslide events of 2008–2009 and

* Corresponding author.

E-mail addresses: dpeduto@unisa.it (D. Peduto), gnicodemo@unisa.it (G. Nicodemo), dluongo@unisa.it (D. Luongo), borrelli@irpi.cnr.it (L. Borrelli), reale.d@irea.cnr.it (D. Reale), sferlisi@unisa.it (S. Ferlisi), fornaro.g@irea.cnr.it (G. Fornaro), giovanni.gulla@irpi.cnr.it (G. Gullà).

2009–2010 have highlighted, among other effects, the impact produced by the increasingly widespread damage to the road network because of the episodic acceleration of several existing landslides (Antronico et al., 2013; Gullà et al., 2012). In the Calabria territory, the interaction of landslides with the road network results in an overload of the regional social-economic gap; recently, this has suggested the promotion of structured knowledge on landslides throughout the use of National Recovery and Resilience Plan (NRRP) founds (<https://www.italiadomani.gov.it/content/sogei-ng/it/en/home.html>).

A road interacting with an unstable slope typically requires additional monitoring (Donnini et al., 2017; Ferlisi et al., 2021; Gullà et al., 2004a, 2004b) and (ordinary/extraordinary) maintenance activities to avoid interruptions to vehicle circulation. These activities, if carried out on a regular basis, depend on various factors (e.g. the road type and the average daily traffic, the type of landslides and the involved geo-materials) and the extra-costs are rarely affordable by the road manager, who may need to prioritize the road stretches where the monitoring/maintenance works can no longer be postponed. The drawbacks of this frequent solution bring along the progressive reduction of the functionality – or even the abandonment – of (some primary and many secondary) roads in inner hilly/mountain areas, therefore further contributing to the continuous depopulation that many areas of central-southern Italian Apennines have been experiencing for the last decades. Consequently, the need for easy-to-transfer/apply procedures for slow-moving landslide risk analysis becomes more and more urgent to support informed decision-making.

As for the analysis of the risk posed by landslides on the infrastructure network, passing from analyses at small (i.e. 1:100,000) to medium (i.e. 1:25,000) and to large (i.e. 1:5000) scale, the need of quantitative information increases, and more detailed data with higher resolution are necessary (Ferlisi et al., 2019; van Westen et al., 2008; Winter and Wong, 2020). Accordingly, small- and medium-scale analyses may be performed within a qualitative framework, whereas large-scale analyses (a fortiori on a detailed scale, i.e. > 1:2000) require a quantitative approach. The key difference between the two approaches is that whereas qualitative risk analysis mainly relies on indices, nominal (e.g. low, moderate and high) or numerical scales, on the other hand Quantitative Risk Analysis (QRA) quantifies a given level of loss with its probability and associated uncertainties (Corominas et al., 2014). Importantly, under the perspective of practical applications, QRA enables the inherent limitations of the results of landslide risk analysis conducted on a qualitative basis to be overcome (Caleca et al., 2022; Corominas et al., 2014; Gullà et al., 2021; Lu et al., 2014; Winter and Wong, 2020; Zhang et al., 2023; Zhou et al., 2024). This is the case in Italy, where current legislation (Law 365/2000, in compliance with the Decree of the President of the Council of Ministers of 29 September 1998) leads to official landslide risk zoning maps that, although useful for land-use planning purposes, are not suitable for (Ferlisi and De Chiara, 2016; Ferlisi et al., 2016): i) the prioritization of areal or linear elements classified at the same level of risk (e.g. very high) that require mitigation measures and the related allocation of financial resources; ii) the selection of the most appropriate risk reduction strategy (including the type and size of either prevention or protection works).

The analysis of the expected consequences to the roads represents a key step in landslide risk management. It involves of the identifying the exposed road stretches and estimating their physical vulnerability with related repair/replacement costs. In quantitative terms, physical vulnerability can be expressed by a relationship between the parameter representative of the landslide intensity and the expected damage or propensity for loss (Corominas et al., 2014; Galli and Guzzetti, 2007; Luo et al., 2023; Peduto et al., 2017, 2018b; Winter et al., 2016). The intensity parameter of a given landslide type relates to its destructiveness power; for slow-moving landslides, in the scientific literature (and in the present work) differential or total displacements are commonly used (Corominas et al., 2014; Fell et al., 2008; Mavrouli et al., 2019; Nappo et al., 2019; Peduto et al., 2017).

The estimation of the effects on the road (at medium and large scales) requires in situ surveys to collect inventories wherein damage severity levels are classified according to qualitative systems, such as the one based on the visible damage recorded to the road pavement (Ferlisi et al., 2021; Mavrouli et al., 2019; Nappo et al., 2019). Then, coupling the damage severity level with the pertaining value of the landslide intensity parameter represents the input data for the generation of probabilistic tools such as empirical fragility and vulnerability curves (Ferlisi et al., 2019; Fotopoulos and Pitilakis, 2013; Nicodemo et al., 2018; Peduto et al., 2017; Zhang and Ng, 2005).

Carrying out QRA for roads can be challenging due to the plenty of required data (Mavrouli et al., 2019). Today, various remote sensing techniques (e.g. optical or acoustic measurements, laser scanner, drones) can support the design, monitoring and maintenance planning of linear infrastructures, while being non-invasive and, most of all, cost-effective for analyses over large areas. In the last decades, displacement measurements derived from the Differential Interferometric processing of Multitemporal Synthetic Aperture Radar images (MT-DInSAR) have become a well-established complement to the aforementioned techniques. MT-DInSAR data, in fact, provide high-resolution measurements of ground displacements with millimeter accuracy (on sufficiently long deformation time series) at affordable costs (Frattini et al., 2018; Journault et al., 2018; Noviello et al., 2020; Peduto et al., 2021; Wasowski and Bovenga, 2015). Recently, Reinders et al. (2022) examined the compliance of MT-DInSAR data with geotechnical design codes and their applicability in the field of transportation geotechnics by highlighting that these data can support and complement with other conventional techniques in the different stages of the project as per the Eurocode-7. Fan et al. (2024) proposed an integrated use of MT-DInSAR, geophysical inversion, and numerical simulation for a non-contact quantitative risk analysis to landslides affecting a highway. The availability of very high-resolution SAR sensors (i.e. COSMO-SkyMed and TerraSAR-X) fostered the use of MT-DInSAR data to analyze the behavior of the infrastructure networks interacting with slow-moving landslides (Cignetti et al., 2023; Ferlisi et al., 2021; Infante et al., 2019; Nappo et al., 2019; North et al., 2017; Reyes-Carmona et al., 2020). Particularly, Ferlisi et al. (2021) pointed out how the combination of MT-DInSAR and damage data is useful for QRA on roads by means of powerful tools such as fragility and vulnerability curves. For this kind of analysis, multi-temporal road damage datasets can help to investigate the response of the infrastructure to slope movements as resulting from a combination of different factors such as the landslide kinematics, the involved geomaterials, the exposed road stretch typology and its position within the landslide-affected area. However, a continuous updating of the information on the maintenance state of all roads (including not primary trunks) can be expensive, thus it typically relies on warnings by road users or local technical officers.

For studies at large scale, Google Street View imagery, whose coverage is increasing worldwide, can be used to collect multi-temporal photos of the road pavement and side structures (Nappo et al., 2019; Ferlisi et al., 2021; Pecoraro et al., 2023); for more detailed analyses, the use of UAV-based photogrammetry products for semi-automatic detection and classification of asphalt road damage in landslide-affected areas allows overcoming the subjectivity of traditional visual inspections of the road pavement (Nappo et al., 2021).

Under the perspective of a sustainable risk management and informed decision process, the present study proposes a multi-source based approach that exploits background knowledge (i.e. geological-geomorphological data, geotechnical monitoring and characterization, ground-based monitoring techniques, results of in-situ surveys), remote sensing data (i.e. MT-DInSAR and Google Street View images) and probabilistic tools (i.e. fragility and vulnerability curves) to quantitatively estimate the risk to roads. These curves, retrieved via procedures widely adopted in literature (Ferlisi et al., 2021; Negulescu et al., 2014; Peduto et al., 2018b, 2019; Pitilakis and Fotopoulos, 2015), allow forecasting the expected damage by taking into account inherent

uncertainties related to the used datasets (e.g. information gathered from damage surveys; the aforementioned factors presiding over damage occurrence including the maintenance activities on the road).

The method is tested in a well-studied area affected by slow-moving landslides and crossed by the Statal Road SS660, which represents the primary connection to Acri town (Calabria region, southern Italy) in southern Italian Apennines.

This study allows enriching the knowledge on the specific case study such as the geometric and lithological typifying of landslides, which is tailored for the analysis of the specific interaction (landslide-road). Importantly, novel aspects with respect to the existing literature on QRA for roads affected by slow-moving landslides are addressed, namely: *i*) an original road damage ranking is defined for analyses at large scale; this looks at the infrastructure as a whole by considering both the condition of the asphalt pavement and the side retaining structures; *ii*) road damage evolution in time was associated with the landslide-induced cumulative displacements in between two repair works to analyze the effects of the mechanical interaction of the road with the unstable slope; *iii*) empirical fragility and vulnerability curves – specifically designed for the infrastructure under study via the combined exploitation of multi-source remote sensing data (MT-InSAR and Google Street View imagery) and results of in-situ surveys – are generated to forecast the economic losses pertaining to the whole road stretch, should no countermeasures be taken for landslide risk mitigation in a fixed time scenario.

2. Materials

2.1. Geological, geomorphological, and geotechnical settings

The study area, located along the western border of the Sila Massif (northern Calabria), falls within the middle portion of the Mucone River basin and includes the town of Acri (Fig. 1). The climate is Mediterranean with dry summer and precipitation concentrated during mild winters (Terranova et al., 2007). The area, ranging in elevation from 300 to 900 m a.s.l., is made by high-grade metamorphic rocks of Palaeozoic age, intruded by granitoid rocks (Fig. 1a). Since the Late Miocene, crystalline rocks experienced intense weathering processes, resulting in a complex and deep weathering profile (Borrelli et al., 2007; Borrelli et al., 2014b).

The metamorphic rocks are found in the central portion of the area, along the slopes carved by the main watercourses (e.g., Mucone River and Calamo Stream), and consist of biotite-garnet and sillimanite gneiss. The granitoid rocks outcropped in the eastern and northwestern portions of the area and mainly consist of tonalite. Old fluvial conglomerates (Upper Pleistocene) interbedded with coarse sand and mud occurred close to Acri town, whereas recent alluvial deposits (Holocene) are found along the riverbeds (Fig. 1a).

The Acri area presents a complex structural setting because several thrust faults, formed under a compressive regime during the Miocene, and Early Pleistocene NW–SE-trending left-lateral strike-slip faults, associated with a transpressive regime, have been dissected by high-angle N–S-trending normal faults during the middle-upper Pleistocene (Borrelli et al., 2014b) (Fig. 1a).

Moreover, compressive, tensional and/or strike-slip fault movements have dislocated inherited weathering profiles (Borrelli et al., 2014b) creating a complex assemblage of weathering horizons and substantially increasing the state of fracturing in the rock masses (Borrelli and Gullà, 2017). Along the major fault planes, very wide fault damage zones occur, with an occasional thick argillification of the fault cores that reaches the maximum thickness along the main low-angle thrust faults (Borrelli and Gullà, 2017). The Quaternary tectonic uplift, responsible of a morphology characterized by steep slopes and deep, narrow valleys (e.g., Mucone, Calamo, and Ceraco), and the intense weathering processes affecting the rock masses strongly favor mass movements development in the study area (Borrelli et al., 2007; Borrelli et al., 2014b).

Particularly, landslides (e.g., slide-debris flows, debris slides, and rock slides) and Deep-Seated Gravitational Slope Deformations (DSGSDs) are widespread along the slopes that border the Mucone River and its tributaries, where the local relief energy, steep slopes, and gravitational landforms are commonly associated with faults and related fault zones (Fig. 1a).

According to the maximum thickness of the involved material, which was estimated on a geomorphological basis, three categories of landslides (shallow, medium-deep, and deep-seated) can be distinguished (Borrelli and Gullà, 2017), as shown in Fig. 1b. Particularly, shallow landslides of slide and slide-flow types generally affect detrital-colluvial covers. They have failure surfaces located at a depth up to about 3 m, a width ranging from 5 m to 60 m and a total length that is strongly influenced by their evolution. Indeed, after the landslide triggering, the phenomenon can stop or evolve into a debris flow. Medium-deep landslides, generally of slide type, involve soil-like rocks and/or weakly weathered rocks (i.e., slope debris, colluvial soils, residual soils and gneissic rocks from completely to moderately weathered). They are characterized by failure surfaces reaching a depth up to approximately 30 m, a width approximately ranging from 50 m to 200 m and a length varying from 100 m to 350 m. Deep landslides, generally translational slides, involve fresher rocks (i.e., gneissic rocks from completely to slightly weathered) and show a strong tectonic constraint. Particularly, the geometry of landslide bodies is dissected by high-angle faults, while thrust faults generally control the development of landslide failure surfaces. They are characterized by failure surfaces deeper than 30 m; their width approximately ranges from 200 m to 500 m and their length from 300 to 800 m.

In addition, two large DSGSDs of Sackung-type (Serra di Buda and Serricella-Croce di Baffi) affect the study area (Fig. 1b). These DSGSDs, with a depth equal or higher than 200 m, have respectively a length of about 1.2 km and 1.5 km; a width of 3 km and 2 km and a surface of 3 km² and 1.5 km². The typical features of these phenomena, partially obliterated by shallow, medium-deep and deep landslides that are superimposed on them, are summit crown-shaped scarps, terrace-like flats, convex slope profiles, and foot protrusions towards the bed of the watercourses (Borrelli and Gullà, 2017). From the geotechnical point of view, the geomaterials produced by weathering and degradation processes of the gneissic rocks in the study area and in similar geological context can be framed among residual-colluvial soils to saprolitic soils (Cascini and Gullà, 1993; Gullà et al., 2003); their connection with tectonic sub-horizontal structures favor the formation of deep-seated failure surfaces, as in the case of Serra di Buda DSGSD. Referring to Cascini and Gullà (1993) and Gullà et al. (2020), the completely degraded gneiss, which is the geomaterial of main interest for deep-seated landslides, exhibits reference values of the friction angle ranging from 23° to 35° at the peak shear strength and from 17° to 31° at the residual shear strength, with associated intercept cohesion values respectively ranging from 28 to 100 kPa and from 0 to 40 kPa. For the heterogeneous weathered and degraded geomaterials involved in the deep-seated landslides, a value of 22 kN/m³ can be assumed as representative of the natural unit weight.

2.2. Monitoring data

In the study area, starting from 1998 to 99, a conventional monitoring network was installed by the Research Institute for Geo-Hydrological Protection – National Research Council of Italy (IRPI-CNR), (Gullà et al., 2004b; Gullà, 2014). Its initial objective was the safe reopening of the SS660 road affected by the Serra di Buda DSGSD mobilization. Focusing on instruments aimed at measuring ground displacements, the monitoring network consisted of (Fig. 2): GPS, quadrilaterals and total stations, inclinometers (Dei Cas et al., 2021). Later, this network was integrated with ground surface displacement time series achieved from the processing of multi-sensor SAR images with interferometric techniques (MT-DInSAR), spanning

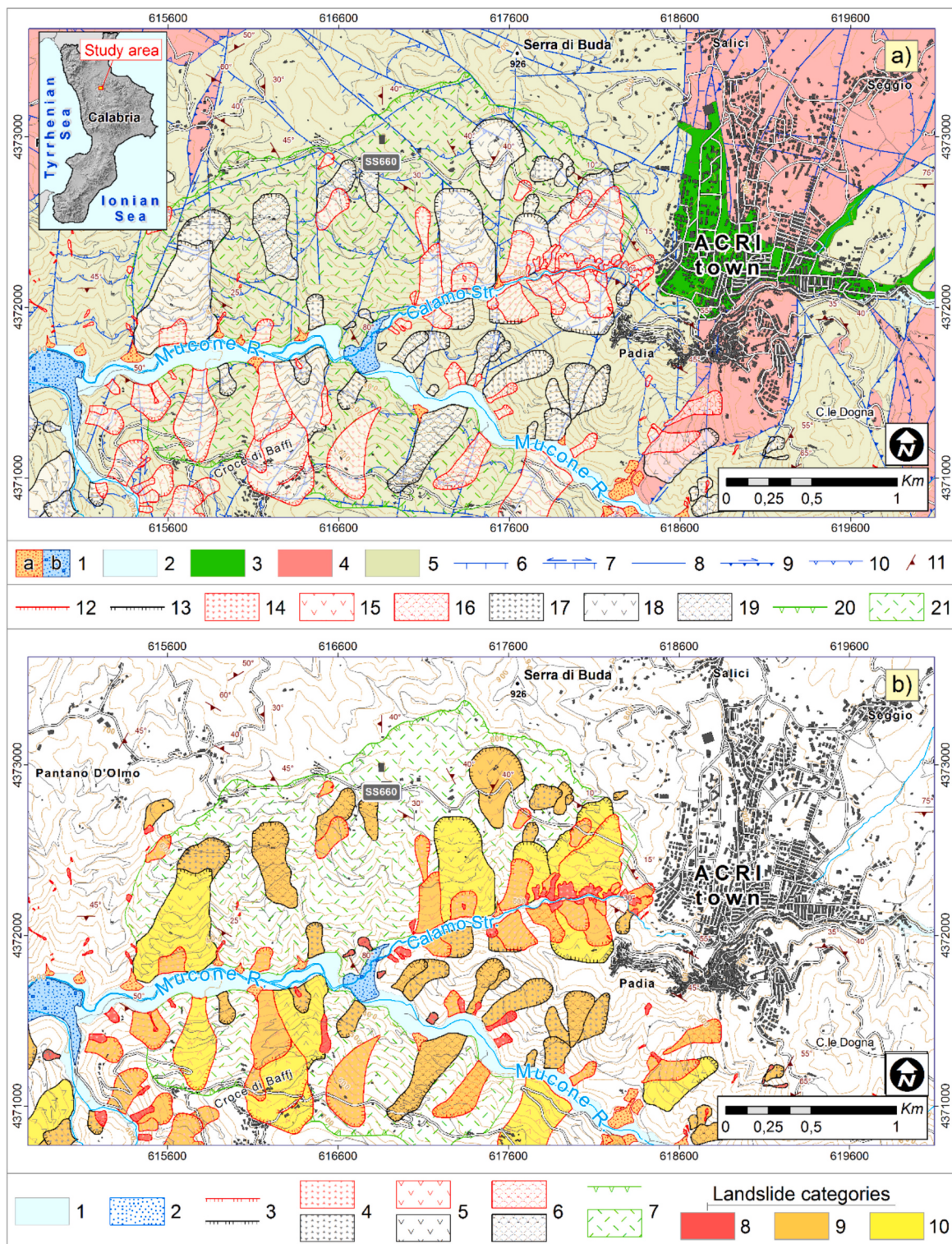


Fig. 1. The study area: a) geological setting and b) landslide inventory (from Borrelli and Gullà, 2017, modified). Legend a): 1) debris cones (a) and alluvial fans (b) (Holocene); 2) alluvial deposits (Holocene); 3) fluvial conglomerates (Upper Pleistocene); 4) granitoid rocks (Palaeozoic); 5) biotite-garnet and sillimanite gneiss (Palaeozoic); 6) normal fault; 7) left- or right-lateral transcurrent fault reactivated as a normal fault; 8) fault with undetermined kinematics; 9) high-angle transpressive thrust; 10) low-angle thrust; 11) metamorphic layering; 12) active landslide scarp; 13) dormant landslide scarp; 14) active debris slide; 15) active rock slide; 16) active slide/debris flow; 17) dormant debris slide; 18) dormant rock slide; 19) dormant slide/debris flow; 20) DSGSD scarp; and 21) DSGSD body. Legend b): 1) alluvial deposits; 2) debris and alluvial fan; 3) landslide scarps (active and dormant); 4) debris slide (active and dormant); 5) rockslide (active and dormant); 6) slide/debris flow (active and dormant); 7) DSGSD (scarp and body); 8) shallow landslide; 9) medium-deep landslide; and 10) deep landslide.

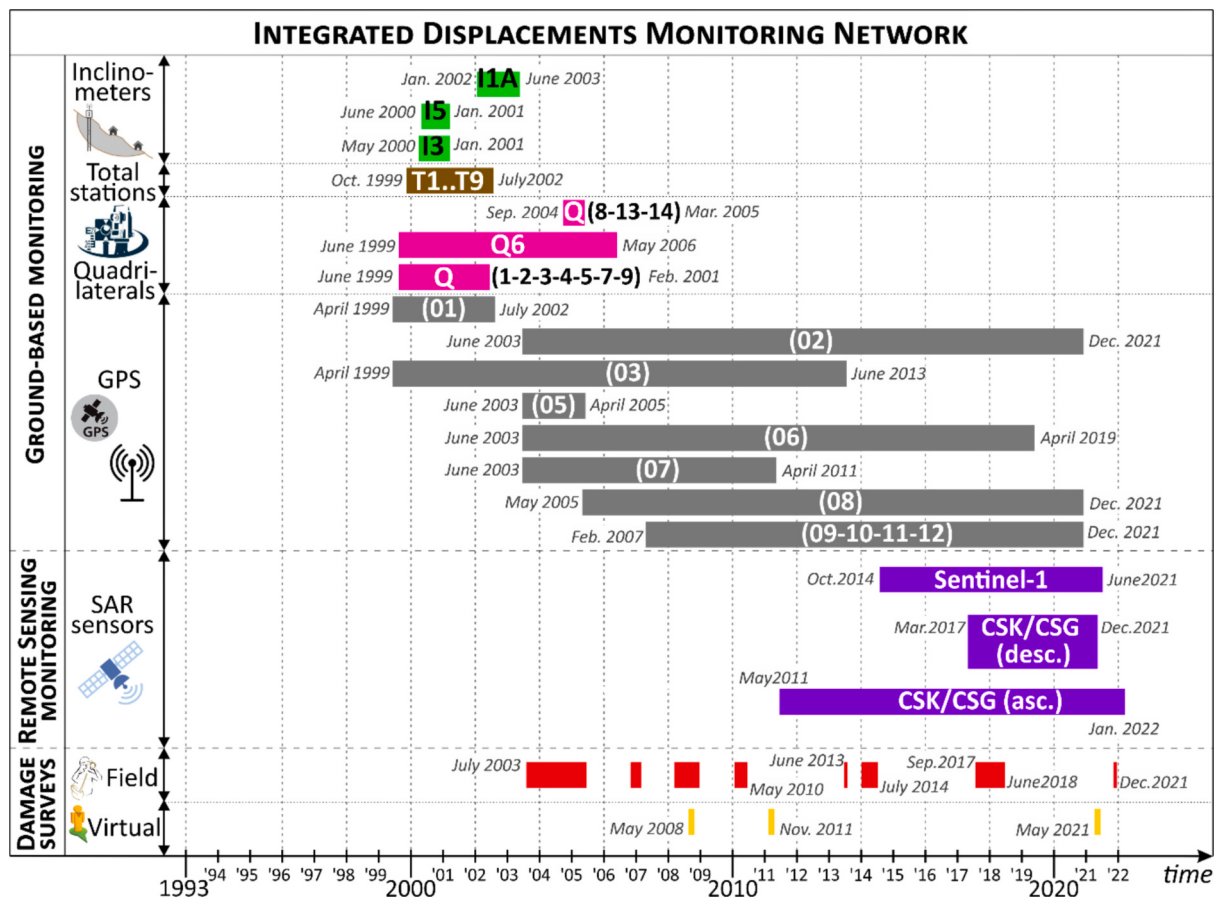


Fig. 2. Integrated multi-source displacement monitoring network available for the study area including ground-based (inclinometers, total stations, quadrilaterals and GPS) monitoring, multi-sensors remote sensing MT-DInSAR data and multi-temporal damage (field and virtual) surveys. CSK, CSG stand for COSMO-SkyMed and COSMO-SkyMed Second Generation, respectively.

from October 2014 to January 2022.

2.2.1. Geotechnical ground-based monitoring

The GPS network over the entire study area is shown in Fig. 3a; five out of eleven working stations concentrate in an active rockslide-affected area (i.e. 01, 02, 03, 07, 08, see Fig. 3b). Here, 3 inclinometers (I3, I5, I1A), 9 benchmarks detected by the total stations and 11 quadrilaterals can also be found (Fig. 3b). Except for GPS, ground-based monitoring systems stopped being operative in 2013. Table 1 summarizes the information concerning the ground-based monitoring network installed over the study area.

2.2.2. Remote sensing monitoring

Multi-sensor SAR dataset consisting of high-resolution C-Band Sentinel-1 and of very high-resolution X-Band COSMO-SkyMed/COSMO-Skymed Second Generation (CSK, CSG) acquisitions were analysed. For each sensor, acquisitions from both ascending and descending passes were exploited (Fig. 2). Specifically, the Sentinel-1 dataset, acquired in the Interferometric Wide-Swath (IW) mode, includes 341 images acquired on ascending orbits (relative orbit number 44) from 08/10/2014 to 27/06/2021, whereas the descending dataset (relative orbit number 124) includes 335 images acquired from 14/10/2014 to 27/06/2021. For the aim of the study concerning a limited extent in west-east direction, only one of the available swaths in the Sentinel-1 standard slice was processed for each orbit direction, specifically the IW3 for the ascending track and the IW1 for the descending track, corresponding to an average incidence angle at scene center of about $\sim 44^\circ$ (ascending track) and $\sim 34^\circ$ (descending track).

Conversely, the very high resolution X-Band dataset acquired in the

Strimap mode, corresponding to a spatial ground resolution of about ~ 3 m, includes 162 images acquired on ascending orbit (Beam H4-01, corresponding to an incidence angle at scene center of $\sim 27^\circ$) from 27/05/2011 to 23/01/2022 and 51 images on descending orbit (Beam H4-03, corresponding to an incidence angle at scene center of $\sim 29.5^\circ$) in a shorter period from 03/03/2017 to 25/12/2021.

After the initial procedures aimed at generating the stacks of co-registered acquisitions, each dataset was processed through the two-step MT-DInSAR processing strategy described in Fornaro et al. (2014). The method is based on a sequence of a low (small-scale) and high-resolution (large-scale) processing of interferometric SAR data acquired over repeated passes. The low-resolution processing exploits the SBAS method described in Fornaro et al. (2009) and provides the estimation of both the atmospheric disturbance and the small-scale non-linear deformation. This estimation allows implementing the data phase calibration for the subsequent full-resolution analysis, which is performed by applying the Differential Tomography (Fornaro et al., 2014) to the calibrated stack to detect and estimate the parameters of interest (i.e. residual topography and residual deformation rate) at full resolution of targets, referred to as Persistent Scatterers (PS), whose electromagnetic backscattering is sufficiently coherent over all the period spanned by the image dataset. Small- and large-scale deformation components are then combined to provide the final large-scale deformation time series.

Fig. 4a-d show the distribution of the detected PS and the estimated velocity (V_{LOS}) along the radar sensor line of sight (LOS). Results shows a good agreement of the results coming from the processing of different sensor datasets, i.e. Sentinel-1 and CSK/CSG, acquired along the same orbit direction. Unfortunately, the area of interest is largely

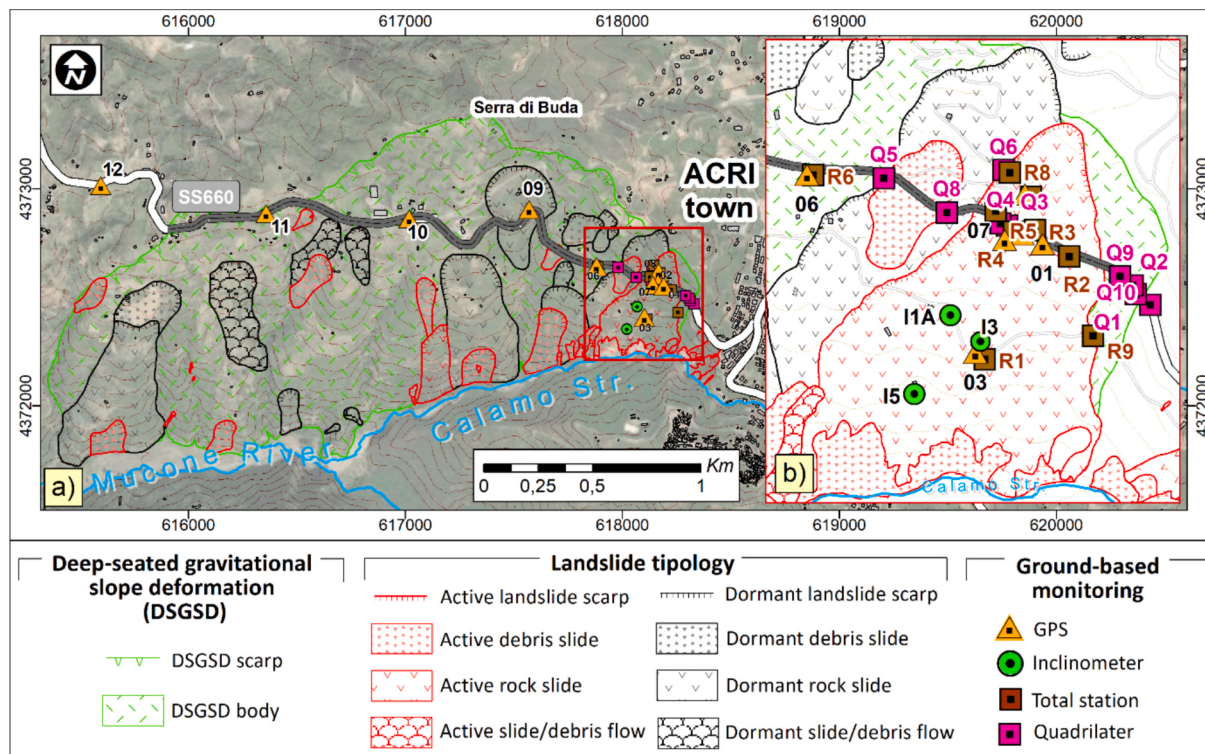


Fig. 3. a) Ground-based displacement monitoring network within Serra di Buda DSGSD with b) close-up view of the in-depth monitored active rock slide after the reactivation of 1998–99.

Table 1
Main characteristics of the installed ground-based displacement monitoring network.

Measure type	Instrument	Number of installations	ID number	Installation depth from ground-level
Surface displacements	GPS	11	01-02-03-05-06-07-08-09-10-11-12	-
	Quadrilaterals	11	Q1-Q2-Q3-Q4-Q5-Q6-Q7-Q8-Q9-Q10-Q13	-
	Total stations	9	T1-T2....T9	-
Deep displacements	Inclinometers	3	I3 I5 I1A	98 m 63 m 152 m

characterized by the presence of vegetation that limits the final density of PS, which are mostly located on built areas and roads.

It is widely known that MT-DInSAR is sensitive to the projection of the actual ground deformation on the LOS, this latter being usually mostly oriented in West East direction with a very small component in the North direction and with an offset with respect to the vertical direction related to the incidence angle (Cascini et al., 2010). Accordingly, the system has a very small sensitivity with respect to North-South components of the ground deformation: the magnitude of the measured LOS deformation in the area of interest could be thus limited because most of the landslides are almost oriented in North-South direction (see Fig. 4a-d).

2.3. Exposed elements and damage surveys

The SS660 road consists of a 7 m-wide single carriageway with two traffic lanes. Like many roads on the hills and mountains in the study area, most of the road track is cut-and-fill type with no (or very limited) footways. In Fig. 5 three simplified sketches of the typical typology of retaining structures along SS660 road are shown. Particularly, the up-slope retaining structures mainly consist of low-rise concrete gravity walls (Fig. 5a) and L-shaped reinforced concrete walls (Fig. 5b). Some downslope road borders are retained by anchored bulkheads (Fig. 5c), which were built as risk mitigation works in correspondence of road

stretches where slope instabilities had previously occurred. Since 2003, IRPI-CNR carried out several in-situ surveys to monitor the conditions of the SS660 road (Fig. 2). For the purpose of the present study, several photos of the road taken over the time were arranged in an archive covering approximately 20 years (some photos are reported in Figs. 7 and 8).

3. The method

The method consists of four phases (see Fig. 6) aimed at pursuing different cascading goals. Phase I addresses landslide typifying by merging geological-geomorphological-geotechnical information, the available landslide inventory map, and both ground-based and remote sensing monitoring data, which previously are crosschecked for an accuracy test. The goal of phase II is the multi-temporal analysis and classification of the damage severity recorded to the exposed elements. For this purpose, first the exposed road stretch is identified; then, the damage severity is collected based on three different sources such as archive photos, in-situ surveys and Google Street-view archive imagery and classified based on a specifically defined damage ranking scale. In Phase III, the landslide intensity parameter is assumed as the cumulative MT-DInSAR-derived displacement computed from the along-slope velocity (V_{slope}) in a fixed period, then associated with the multi-temporal damage severity level to derive empirical cause-effect relationships (i.e.

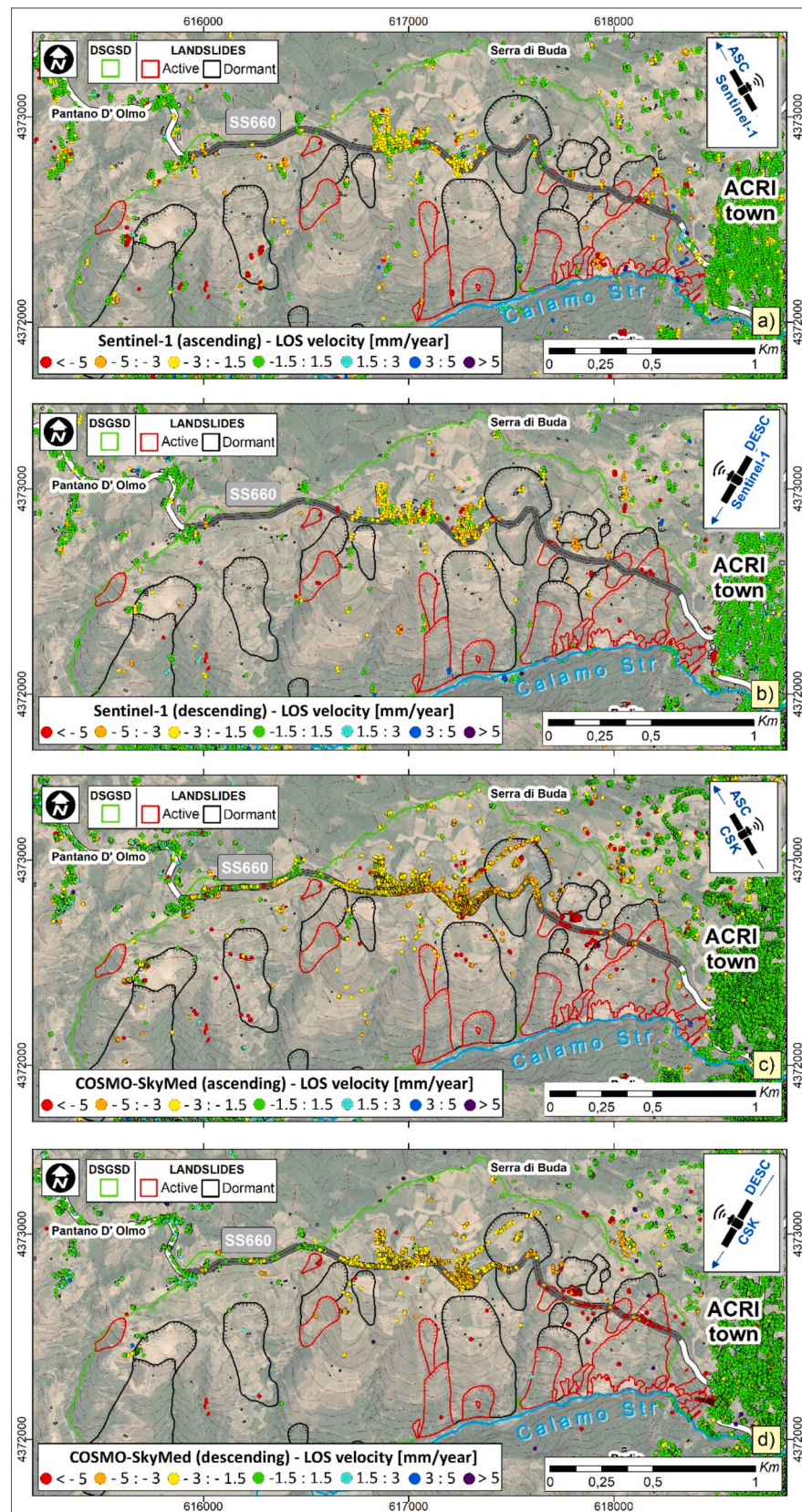


Fig. 4. Multi-sensor remote sensing MT-DInSAR data: Sentinel-1 on a) ascending (period 08/10/14–27/06/21) and b) descending (period 08/10/14–27/06/21) orbits; COSMO-SkyMed on c) ascending (period 27/05/11–23/01/2022) and d) descending (period 03/03/2017–25/12/2021) orbits.

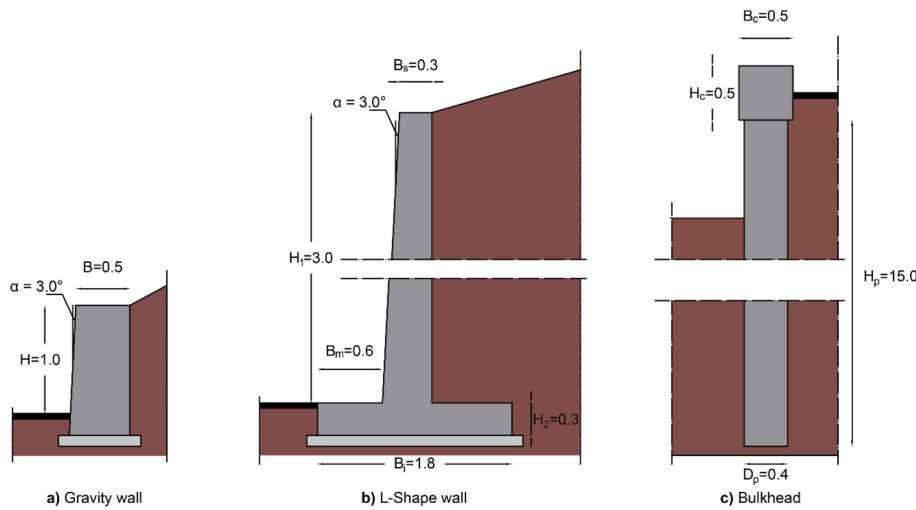


Fig. 5. Sketches of typical retaining structures along the SS660 road: a) a concrete gravity wall; b) L-shaped reinforced concrete wall; c) sheet wall. The size of the structure is expressed in meters and is meant as average values of the structures along the SS660 road.

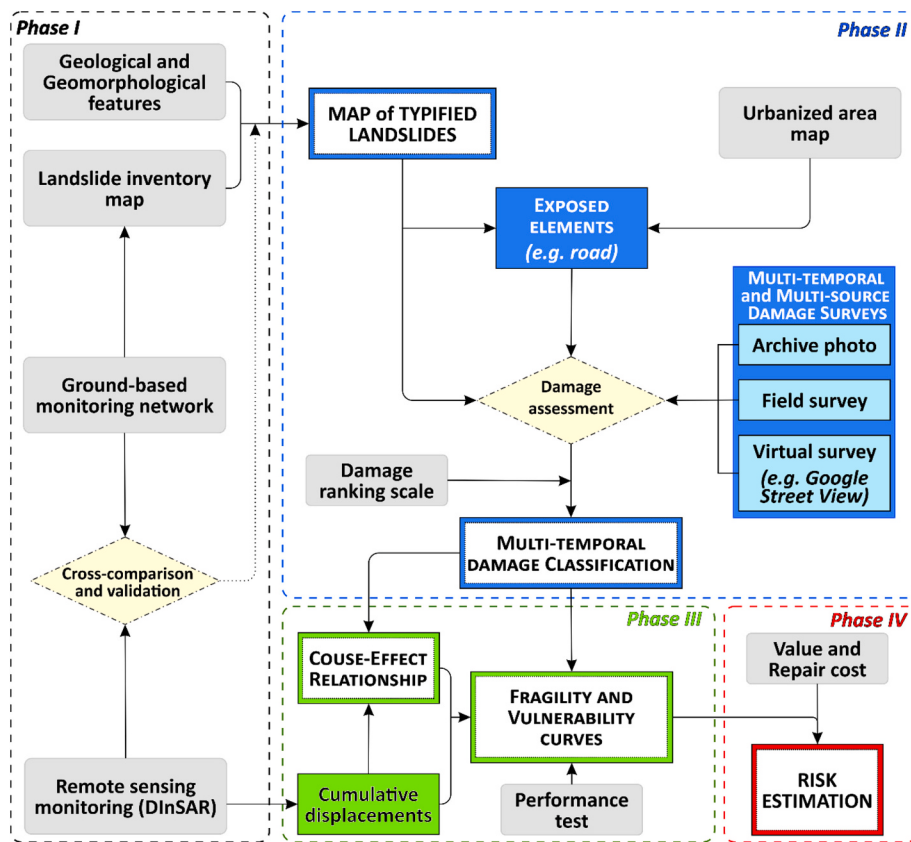


Fig. 6. Flowchart of the adopted procedure.

cumulative displacement vs. damage severity level). These latter allow deriving probabilistic tools such as fragility and vulnerability curves pertaining to the analysed road stretches. In Phase IV, the risk to the road is estimated in term of repair costs (or economic loss) for a fixed scenario.

3.1. Phase I: data accuracy test and landslide kinematic characterization

Preliminarily, the accuracy of the available MT-DInSAR data was assessed via a comparison of both Sentinel-1 and CSK/CSG datasets

(Fig. 4) with the available GPS data (Fig. 3). For this purpose, the vertical (Z) and horizontal (North and East) components acquired by the GPS benchmarks were projected along the LOS of the PS taken as reference for the comparison. Eq. (1) was used:

$$\text{GPS}_{\text{LOS}} = d_N \times \text{LOS}_N + d_E \times \text{LOS}_E + d_Z \times \text{LOS}_Z \quad (1)$$

where d_N , d_E , d_Z are the three components of the GPS displacement vector d_{GPS} , and LOS_N , LOS_E , LOS_Z are the direction cosines of the LOS vector, i.e. they specify the LOS unit vector, pertaining to the analysed SAR sensor (i.e. Sentinel-1 and COSMO-SkyMed). To carry out the

comparison, the PSs were chosen according to their coherence (maximum) and relative distance (minimum) with respect to the GPS points.

Furthermore, considering that MT-DInSAR datasets are constrained along a given movement direction (i.e. 1D-LOS) and for the study area datasets from two different SAR sensors (on both ascending and descending orbits) were available, the velocity values were projected from the LOS to the steepest slope direction following the procedure proposed by Cascini et al. (2010). This allowed interpreting the kinematics of a given landslide, independently from the different sensor analysed. Then, considering that the LOS projection on the along-slope direction can be biased by errors (Cascini et al., 2010; Colesanti and Wasowski, 2006), a threshold on the value of the scaling factor (Plank et al., 2010) of each PS, namely the constant value by which the modulus of the LOS velocity (V_{LOS}) must be multiplied in order to obtain the modulus of the along-slope velocity (V_{slope}), was set. As shown by some authors (Cascini et al., 2013; Herrera et al., 2013; Plank et al., 2010), values of the scaling factor lower than 4 allow selecting the most reliable V_{slope} PS values, thus accounting for the limits related to both the sensor acquisition geometry and the local topographic conditions (i.e. aspect and slope angles). Accordingly, the PSs with scaling factor exceeding 4 were not considered in the following operations.

As a key step of Phase I, the landslides mapped in the available inventory were grouped based on their type, geometry, thickness, geo-materials, and kinematics (hereafter called *typified landslides* after Gullà et al., 2017). This latter derived from MT-DInSAR velocity values that were available for most of the landslides mapped in the study area. For this purpose, the mean velocity of landslide bodies ($\bar{V}_{\text{slope_landslide}}$) was computed via the formula proposed by Cascini et al. (2013) (in which weight values were established on the basis of the PS coherence, i.e. the higher the PS coherence the higher the weight value):

$$\begin{aligned} \bar{V}_{\text{slope_landslide}} &= \left(\frac{\sum_{i=1}^N w_{ci} \times V_{\text{slope_i}}^2}{\sum_{i=1}^N w_{ci}} \right)^{1/2} = \left(\sum_{i=1}^N \frac{w_{ci}}{w_{cN}} \times V_{\text{slope_i}}^2 \right)^{1/2}; w_{ci} \\ &= \frac{(1 - \varepsilon_{\min})}{(C_{\max} - C_{\min})} \times (C_i - C_{\min}) + \varepsilon_{\min} \end{aligned} \quad (2)$$

where: i refers to the i -th PS within the boundary of the landslide; N is the total number of PS within the boundary of the landslide; w_{ci} is the coherence weight of the i -th PS within the landslide boundary; w_{cN} is the sum of w_{ci} ; $V_{\text{slope_i}}$ is the velocity along the slope of i -th PS; C_{\max} is the maximum coherence value of the used dataset; C_{\min} is the minimum coherence value of the used dataset; C_i is the coherence value of the i -th PS within the boundary of the landslide; ε_{\min} is a positive number not greater than 1 defining the weight of the PS with the smallest coherence. In the analyses, ε_{\min} value was fixed equal to 0.2 thus assigning a weight of 20 % to the smallest coherence value.

3.2. Phase II: Multi-temporal damage data collection and analysis

The exposed elements (i.e. the road stretches crossing the landslide-affected areas) were identified by overlapping the map of typified landslides on the map of urbanized areas. The damage analysis was carried out by analyzing: *i*) the archive photos obtained since 2003 by the IRPI-CNR during in-situ surveys, specifically in the stretch of SS660 affected by the Serra di Buda rockslide, *ii*) the results of virtual surveys through Google Street view image archive (November 2008, May 2011, May 2021), and *iii*) the results of an in-situ survey carried out on 14 December 2021.

As for the damage severity classification, although in the scientific literature there are several predictive models of asphalt deterioration under normal operating conditions (e.g. Sharp and Booker, 1984), there are few predictive models that relate landslide displacements to the

observed road damage (Mansour et al., 2011; Mavrouli et al., 2019). Starting from the classification of Ferlisi et al. (2021), damage was ranked in four increasing severity levels (Table 2) including, as a novelty, both the asphalt pavement and the side retaining structures (if any) for the cut-and-fill slope sections of the SS660. This allowed assigning the damage severity level to the entire road section (assuming, in a conservative way, the higher level between the road pavement and the side structures).

Thus operating, we overcame the limitations related to the repair works, which, in the study area, are carried out more frequently on the asphalt than on the retaining structures, and may have concealed the effects of slope instability on the infrastructure (Fig. 7).

Ad-hoc prepared monographic fact-sheets (Fig. 8) were filled in by collecting information on the location, the presence of a landslide and its key features, the type of road and the structural typology of the retaining structure, the damage severity level of both the pavement/asphalt and the sidewalls, and some multi-temporal photos.

Starting from the identification of single damaged (or undamaged) sections, the lengths (in meters) of those road stretches exhibiting different levels of damage were computed by dividing in two equal parts the length of the stretch in between two damaged sections and associating each of them with the damage severity level of the closest damaged section in the observation period. For instance, if a road stretch of L length was limited by two damaged sections with different damage levels (say D1 and D2), it was divided into two sub-stretches of equal lengths ($L/2$ per each) and each of them was associated with the damage recorded by the closest damaged section (i.e. one was associated with D1 and the other with D2). This allowed us to pass from a discrete information referred to the single damaged sections to a continuous information associated with the road stretches composing the entire road.

3.3. Phase III: Cause-effect relationship, fragility and vulnerability curves

The results of the multi-temporal damage analysis were used in combination with spaceborne MT-DInSAR data to derive empirical correlations between cause (i.e. cumulative displacements) and effect (i.e. damage severity level). Very high-resolution MT-DInSAR data were examined to select and quantify the landslide intensity parameter (i.e. the cumulative displacement along the slope direction, δ_{slope}) with reference to a fixed observation period. This agrees with Picarelli

Table 2
Level of damage severity to the road pavement and side retaining structures.

Damage severity level	Description of typical damage	
	Road pavement	Side retaining structures
D0 Negligible	Deformation of the road pavement and cracks are absent or rarely visible. Deformations and cracks locally affect the road pavement without affecting its functionality.	Sporadic hair cracks along the entire length of the structure.
D1 Slight	Deformations and cracks substantially affect the road pavement, affecting all or part of the traffic lanes and/or the edge of the road, therefore it is necessary to reduce the speed limits.	Cracks rarely visible on the structure that do not change its strength.
D2 Moderate	Deformations and cracks definitively compromise the continuity of the road pavement, affecting in whole or in part the traffic lanes and/or the roadside, for which traffic restrictions are necessary.	Cracks clearly visible even with expulsion of material that may have compromised the strength of the structure.
D3 Severe	Wide and widespread cracks distributed along the structure and evidence of tilting or sliding that have clearly modified its strength.	



Fig. 7. Examples of typical repair works to the road pavement in the study area. Road section with a) lateral concrete gravity wall lined with stones and b) concrete low-side retaining structure suffering from cracks on both the pavement and side retaining structures (a1 and b1). Roadway restoration (a2 and b2) with reinforcement works (a3 and b3) and new asphalt pavement (a4 and b4); this latter has concealed the evidence of slope instability on the road pavement but not on the side retaining structures.

(2011), who emphasized the role of cumulative displacement (over a given period of time) in the onset and development of damage to exposed facilities rather than the velocity (Mansour et al., 2011). To estimate the intensity parameter, a buffer with a radius of 10 m was drawn around each damaged road section to take into account both the

non-punctual extension of the damage and the resolution of the used SAR sensor (Nappo et al., 2019). For each buffer, the PSs located within its perimeter were selected and the mean slope velocity of the k_{th} buffer ($\bar{V}_{slope,k}$) was computed as the root mean square weighted PS velocity along the steepest slope direction using the Eq. (2) (as proposed by

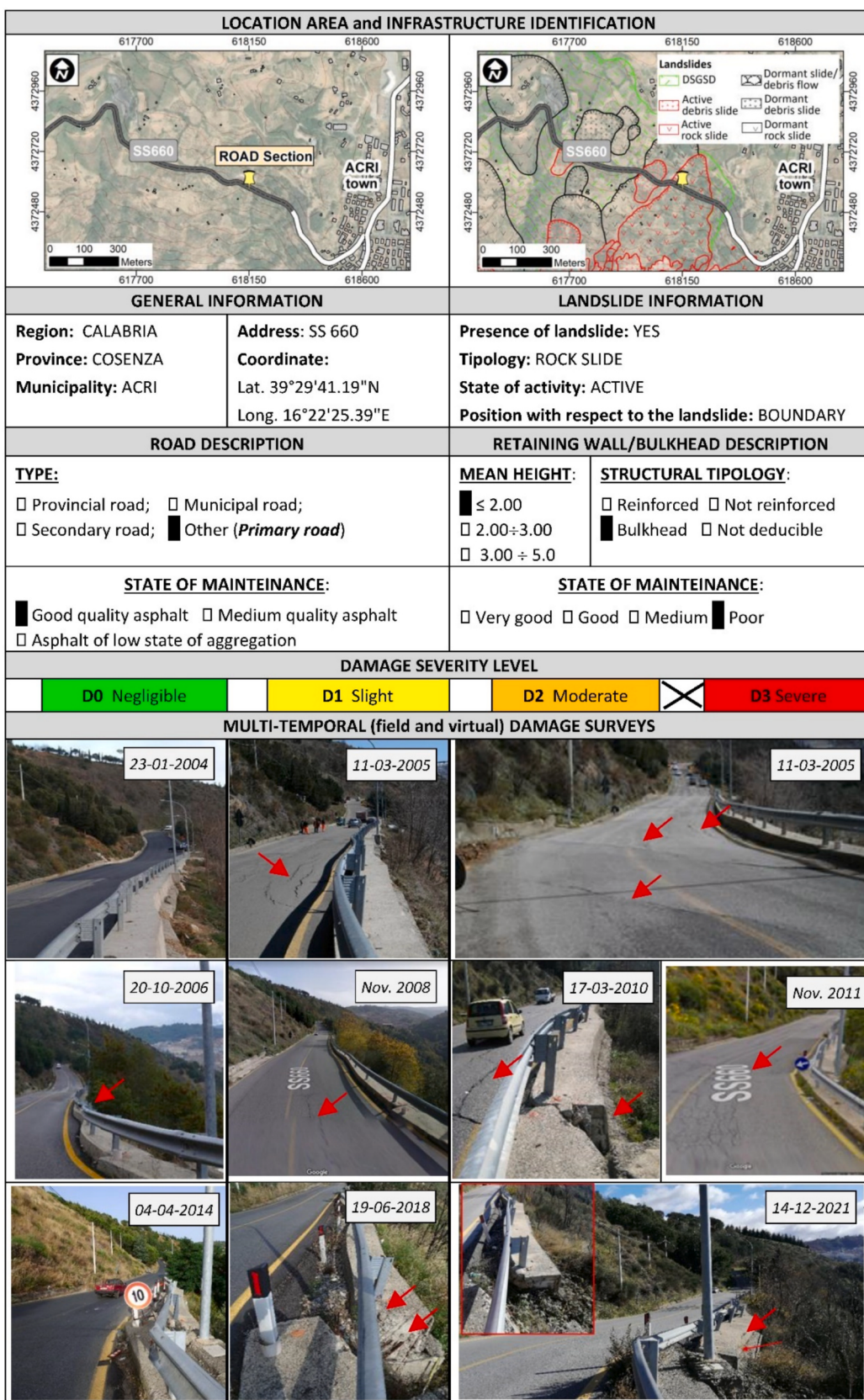


Fig. 8. Multi-temporal (field and virtual) damage surveys: an example of filled road fact-sheet including road pavement and retaining wall/bulkhead damage assessments.

Cascini et al., 2013).

Starting from the $\bar{V}_{\text{slope},k}$ value, the cumulative displacement ($\delta_{\text{slope},k}$) pertaining to k_{th} buffer, in a fixed observation period (t), was computed using the Eq. (3):

$$\delta_{\text{slope},k} = \bar{V}_{\text{slope},k} \times t \quad (3)$$

The computed ($\delta_{\text{slope},k}$) value was associated with the level of damage severity (D_i) assigned to each road section based on the damage classification pertaining to the fixed time interval; thus retrieving the empirical cause (δ_{slope}) vs. effect (D_i) relationship. This latter was then used to generate forecasting tools such as empirical fragility and vulnerability curves by selecting appropriate probabilistic (for fragility curves) and regression (for vulnerability curve) models.

To this aim, the total sample of investigated road sections (i.e., those for which both the landslide intensity parameter and the damage severity level were available) was randomly split into training (70 % out of the total) and testing (30 % out of the total) set.

Then on the training set, based on the analysis of the frequency occurrence of each damage severity level for different classes of the δ_{slope} values, the cumulative log-normal distribution (Negulescu et al., 2014; Peduto et al., 2018b, 2019) and the tangent hyperbolic (Pitilakis and Fotopoulou, 2015; Nicodemo et al., 2020) functions were adopted, respectively, for generating empirical fragility and vulnerability curves.

Specifically, the fragility curves—providing the probabilities $P(\cdot)$ that the damage affecting a section of road can reach or exceed a certain damage severity level (D_i) for a fixed value of the intensity parameter (δ_{slope})—were generated using the Eq. (4):

$$P(\text{Damage} \geq D_i | \delta_{\text{slope}}) = \Phi \left[\frac{1}{\beta_i} \ln \frac{\delta_{\text{slope}}}{\delta_{\text{slope},i}} \right] \quad (\text{with } i = 1, 2, 3) \quad (4)$$

where the fragility parameters associated with the standard normal cumulative distribution function $\Phi[\cdot]$ are the median value ($\delta_{\text{slope},i}$) of the selected intensity parameter (δ_{slope}) and the standard deviation (β_i) of the natural logarithm of the (δ_{slope}) values. These latter parameters, corresponding to the D_i recorded to the road section, were estimated by fitting the empirical data (Ferlisi et al., 2021; Peduto et al., 2019) using the maximum likelihood method (Shinozuka et al., 2003; Fotopoulou and Pitilakis, 2013). In particular, the fragility parameters were obtained maximizing the likelihood (L) function (Eq. 5) by solving Eq. 6 (Shinozuka et al., 2003):

$$L(\overline{\delta_{\text{slope},i}}, \beta_i) = \prod_{j=1}^N \prod_{i=1}^M P_j(\delta_{\text{slope},j}; D_i)^{y_{ji}} \quad (5)$$

$$\frac{d \ln(L)}{d \overline{\delta_{\text{slope},i}}} = \frac{d \ln(L)}{d \beta_i} = 0 \quad (6)$$

where P_j is the probability that the j -th road section (or stretch), belonging to the considered sample and undergoing $\delta_{\text{slope},j}$, will record a D_i ($i = 1, 2, 3$); whereas y_{ji} is equal to 1 or 0 (realization of the Bernoulli random variable) whether the j -th road section (or stretch) sustains or not the $\delta_{\text{slope},j}$ value (Shinozuka et al., 2003).

The vulnerability of the exposed road is herein defined (Corominas et al., 2014; Fell et al., 2008) as the average expected degree of loss due to the occurrence of a slow-moving landslide of given intensity. The expected degree of loss is linked to the expected reversible or irreversible damage on the exposed element that, in turn, can be expressed in term of the repair/replacement costs needed to restore the suffered damage with respect to its original value (Fell et al., 2008; Peduto et al., 2018b; Pitilakis and Fotopoulou, 2015). In this regard, the vulnerability curve can be used to provide a quantitative relationship between the expected average level of damage severity (μ_D) and the cumulative displacement δ_{slope} . In this study, the $\mu_D(\delta_{\text{slope},i})$ values were calculated by adopting the Eq. (7) proposed by Pitilakis and Fotopoulou (2015)

considering for each D_i the discrete probability (P_i) retrieved from the previously generated fragility curves with an associated numerical index d_i (assumed, respectively, as 0.33, 0.66, 1 for D1, D2, D3):

$$\mu_D(\delta_{\text{slope},i}) = \sum_{i=1}^3 P_i \times d_i \quad (7)$$

Then, the vulnerability curves were derived by fitting the $\mu_D(\delta_{\text{slope},i})$ data retrieved by Eq. 7, using the tangent hyperbolic function (Eq. 8) assumed as regression model (Peduto et al., 2018b):

$$\mu_D = a [b + \tanh(c \times \delta_{\text{slope}} + d)] \quad (8)$$

where a, b, c and d are four coefficients determined for the investigated sample of road sections using the least mean square method.

Finally, focusing on the testing set (30 % out of the total) of road sections, the performance of the generated model (i.e., the empirical vulnerability curves) was evaluated by assessing the overall accuracy and other evaluation metrics such as sensitivity, specificity and precision using a 3×3 confusion matrix (Tharwat, 2018; see Fig. 9). The overall accuracy using the predicted classes shows how our classification model is able to predict the class labels given in the problem statement. The sensitivity and specificity are important evaluation metrics of model's ability to recognize positive and negative outcomes of the dataset and are defined as the averages of the "one versus all" statistics. Fig. 9 shows the nine possible outputs of the classification models for the three damage classes D1, D2, and D3. The columns represent the predicted damage severity levels (D_i) derived from the model (i.e., by using the empirical vulnerability curve) and the rows represent the true classes (i.e., in-situ damage severity level recorded during field/virtual survey). In Fig. 9, the TP_{D_i} are the cases for which the classifier predicted the correct D_i -class of the samples; the E_{D_i} are the samples from D_i -class that are misclassified in that class. Thus, the false negative in the D_i -class (FN_{D_i}) is the sum of E_{D_i} , which indicates all the samples that were actually in D_i -class but were misclassified in an incorrect D_i -class; the false positive in the D_i -class (FP_{D_i}) is the sum of E_{D_i} and it indicates all the samples that actually were not in the D_i -class but were misclassified as D_i -class.

3.4. Phase IV: risk analysis

In this phase, the repair unitary cost (RUC) pertaining to the different damage severity level recorded to the road section was first computed. To this aim, the RUC related to different activities required to repair a road suffering from a certain damage severity level (Table 3), was actualized at the starting date of the period considered for the expected damage (ED_i) scenario by using the compound interest formula (Eq. 9):

$$RUC^* = RUC_0^* (1 + r)^t \quad (9)$$

In the Eq. (9) the RUC^* to be referred to the time t^* (in years) can be obtained as the repair unitary cost RUC_0 at the reference year (t_0) amplified or reduced by means of the nominal annual interest rate (r), whose percentage value was evaluated on the basis of data provided by the Italian Institute for Statistics (ISTAT, 2022) about the change in construction costs of roads over time. In Table 3 the considered RUC pertaining to the road pavement (modified after Ferlisi et al., 2021) refer to the date of the last survey (December 2021) considering a nominal annual interest rate ($r = 1.83\%$) referred to the change of construction costs of roads from 2018 to 2021 (ISTAT, 2022). The thickness of different layers refers to secondary suburban roads according to Domenichini et al. (1993); the road width was posed equal to 7 m. As for retaining structures, costs were computed based on the Regional Price List for public civil engineering works of Calabria region (Prezzario Regionale OO.PP. Calabria, 2021) considering, on average, the size of the structures sketched in Fig. 5. The costs refer to the construction of 1 m of the specific structure and were associated only to those sections

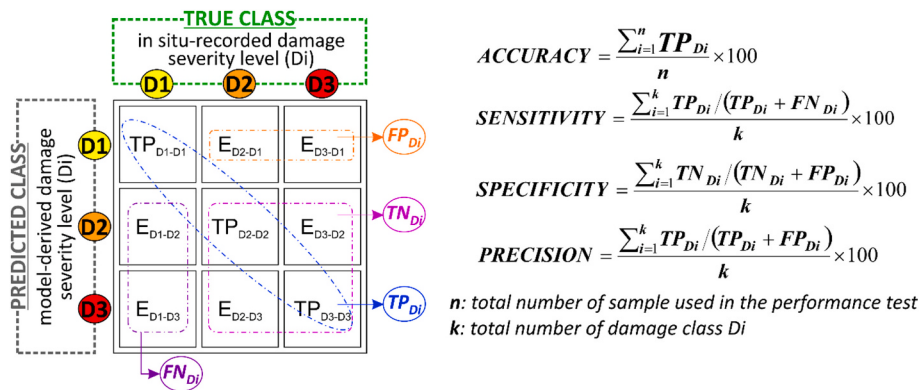


Fig. 9. Confusion matrix for the 3×3 damage class (D_i) validation test carried out using 30 % out of the total road sections jointly with the associated model evaluation metrics (accuracy, sensitivity, specificity and precision). Legend: TP_{Di} = true positive for D_i -class; E_{Di} = misclassified D_i -class for which FN_{Di} and/or FP_{Di} is counted; FN_{Di} = false negative for D_i -class; FP_{Di} = false positive for D_i -class; TN_{Di} = true negative for D_i -class.

Table 3

Activities required for the repair of roads suffering from damage of different severity to the pavement and the side retaining structures.

Repair of road pavement						
Activity	Unit of measure	Cost [€]	Damage severity level			
			D_0	D_1	D_2	D_3
Sealing of cracks in the road pavement	m	4.21	■	—	—	—
Supply and installation of asphalt concrete for wear layer (4 cm thick)	m^3	145.57	—	■	■	■
Milling pavement layers made of asphalt concrete	$m^2 \times cm$	0.44	—	—	■	■
Supply and installation of asphalt concrete for binder layer (5 cm thick)	m^3	132.64	—	—	■	■
Supply and spraying of bitumens modified with elastomers	m^2	0.75	—	—	■	■
Supply and installation of asphalt concrete for base layer (8 cm thick)	m^3	121.90	—	—	—	■
Supply and installation of the road foundation made of stabilised granular mixture (15 cm thick)	m^3	20.34	—	—	—	■
Repair unitary cost (RUC) [€/m]			4.2	40.8	120.4	240.1
Repair of retaining structures			—	—	—	246.5
Gravity wall (formwork, concrete, lean concrete, excavation, drainage material)			—	—	—	—
L-shape wall (formwork, reinforced concrete, lean concrete, excavation, drainage material)			—	—	—	1085.2
Bulkhead (perforation, drilled pile $d = 0.40$ m and $h = 15.0$ m, reinforced concrete)			—	—	—	4185.6

exhibiting a D3 level, considering that in the study area these civil works are not repaired unless they reach a D3 level.

Then, the expected damage (EDi) for each road section in a fixed time was assessed considering different landslide kinematic scenarios. To this aim, the time period for damage forecast was set starting from last repair works to the infrastructure (i.e. at time t_0 the road is undamaged). Within this time interval the four considered damage levels (D0-D3) appear in at least one of the road stretches composing the whole trunk of the analysed road. For each buffer drawn around each damaged road section, δ_{slope} was calculated using Eq. (3), starting from the date of the last repair of the road pavement and assuming a constant \bar{V}_{slope} value in the period for which the monitoring (MT-DInSAR) data were available and three alternative \bar{V}_{slope} values in the time window considered for the damage forecast according to the different landslide kinematic scenarios. Subsequently, by entering the vulnerability curve with the δ_{slope} , it was possible to derive the expected average level of damage (μ_D) for each investigated road section.

Then, the (EDi) scenario was assigned to the pertaining road section based on the value of (μ_D) and the corresponding numerical index d_i (associated with a damage severity level D_i). This value was then extended to the road stretches by considering the portion of road in between two damaged sections as equally divided and associating the level of damage of the closest damaged section (damage length, DL). Finally, the quantitative risk to the road (assumed as the expected monetary loss, EML, in a fixed time scenario) for the entire road trunk analysed was estimated considering the different road stretches with

$$\begin{aligned}
 ACCURACY &= \frac{\sum_{i=1}^n TP_{Di}}{n} \times 100 \\
 SENSITIVITY &= \frac{\sum_{i=1}^k TP_{Di}}{(TP_{Di} + FN_{Di})} \times 100 \\
 SPECIFICITY &= \frac{\sum_{i=1}^k TN_{Di}}{(TN_{Di} + FP_{Di})} \times 100 \\
 PRECISION &= \frac{\sum_{i=1}^k TP_{Di}}{(TP_{Di} + FP_{Di})} \times 100
 \end{aligned}$$

n: total number of sample used in the performance test
k: total number of damage class D_i

their length (DLi), the level of expected damage (EDi) and the repair unit cost RUC_i (€/m) according to the Eq. (10):

$$EML[\text{€}] = \sum_{i=1}^n RUC_i(ED_i) \times DL_i \quad (10)$$

where $i = 1, \dots, n$ is the number of road stretches with a homogeneous EDi.

4. Results

4.1. Phase I

Based on the methodology described in Section 3 (Fig. 6), first GPS and MT-DInSAR data were cross compared in order to assess MT-DInSAR data accuracy. By using Eq. (1) the vertical (Z) and horizontal (North and East) components of displacement acquired by the GPS were projected along the LOS. Both Sentinel-1 and CSK/CSG PSs on ascending and descending orbits were considered referring to the velocity computed over the overlay period (March 2017–December 2021). The different PSs available for each GPS, the differences in the computed average velocity (ΔV) according to the radar sensor and the acquisition geometry, as well as the corresponding mean value ($\bar{\Delta V}$), are summarized in the Supplementary Material (SM) associated with this work; whereas a visual comparison is shown in Fig. 10, wherein the GPS-LOS projected velocity is plotted against the PS LOS-velocity.

As it can be seen, the accuracy of Sentinel-1 (the average ΔV of

Sentinel-1 PS on ascending/descending orbit) is equal to 1.22 mm/year for PS of the ascending dataset and 2.35 mm/year for the descending dataset. Similarly, the accuracy of CSK/CSG is 0.98 mm/year and 0.86 mm/year for the ascending and descending dataset, respectively. For CSK/CSG data, the measured accuracy values fall within the range of 1.5–2.0 mm/year (see Fig. 10) that is reported in the scientific literature (Herrera et al., 2009; Peduto et al., 2018a, 2019).

Then, PS velocity values were projected from the LOS to the steepest slope direction following the procedure proposed by Cascini et al. (2010) (see also Section 3.1). Fig. 11a and b show the map of projected V_{slope} vectors for both Sentinel-1 and COSMO-SkyMed radar sensors. Only PSs with the scaling factor below the threshold of 4 were considered. The maps highlight a good coverage of projected PSs. Specifically, 526 PSs for Sentinel-1 dataset and 2744 PSs for CSK/CSG over the entire landslide-affected area and 189 PSs for Sentinel-1 and 1750 PSs for CSK/CSG dataset over the SS660 were identified.

Fig. 11c shows the map of landslides with indicated the velocity obtained by considering the MT-DInSAR Sentinel-1 and CSK/CSG available datasets. Since the latter referred to different acquisition periods, in order to have coherent information on the landslide kinematics, the mean velocity was determined over the maximum overlap period (March 2017–December 2021) for each PS. In particular, the $\bar{V}_{slope_landslide}$ value was computed using the Eq. 2 and assigned to each landslide body.

Then, starting from the landslide inventory map reported in Borrelli and Gullà (2017) and focusing on the Serra di Buda DSGSD, a GIS attribute table was compiled for each landslide mapped within the DSGSD perimeter. The table sums up all the attributes considered for each landslide that are: ID code, type, state of activity, length, width, area, landslide category, involved geomaterials (Table 4).

Fig. 12 shows a synthesis of key features of typified landslides. Particularly, we used: landslide type (slide; complex (i.e., slide-flow)) and DSGSD; the category of landslide based on the maximum landslide thickness identified on geological and geomorphological base

(shallow landslide (SL), medium-deep landslide (MDL), deep landslide (DL)), and considering the Serra di Buda DSGSD in DL category; the involved geomaterials defined by geological/lithological field surveys and geotechnical investigations (Gullà et al., 2003; Borrelli and Gullà, 2017). Furthermore, the above-mentioned key elements were integrated with the $\bar{V}_{slope_landslide}$ retrieved by the combined use of Sentinel-1 and CSK/CSG datasets (see Table 4).

The DSGSD (49), which affects the entire geological context under consideration, shows $\bar{V}_{slope_landslide}$ values ranging from 5.0 to 10.0 mm/year; this is in agreement with previous studies (Borrelli et al., 2017) and with the data acquired by GPS 09, 10, 11 (Fig. 3). Furthermore, the $\bar{V}_{slope_landslide}$ landslide velocity retrieved by the combined use of Sentinel-1 and CSK/CSG datasets (Fig. 11c) shows that the landslide bodies (35, 43, 44), classified as dormant in the inventory map (Fig. 1), have mean velocities between 10.0 and 15.0 mm/year. As for landslide bodies classified as dormant in the inventory map (Fig. 1), those labelled with (38, 46, 48) have a mean velocity > 15.0 mm/year, whereas the landslides (33, 45, 47) record velocity values ranging from 5 to 10 mm/year. Finally, in agreement with geomorphological outcomes, the combined use of Sentinel-1 and CSK/CSG datasets confirms the state of activity of the Serra di Buda rockslide (23) showing a mean velocity > 15.0 mm/year.

4.2. Phase II

Phase II was aimed at collecting and analyzing the multi-temporal damage severity levels recorded to the SS660 road. This latter was affected over the years by several landslide reactivations that induced repeated closures and road surface replacement interventions. The analysed stretch interacts along 2775 m with a DSGSD (maximum thickness of over 100 m) overlaid by shallower slope instabilities (see Fig. 1b). A multi-temporal analysis of the damage was conducted based on the classification and surveys reported in Section 3.2. Referring to the

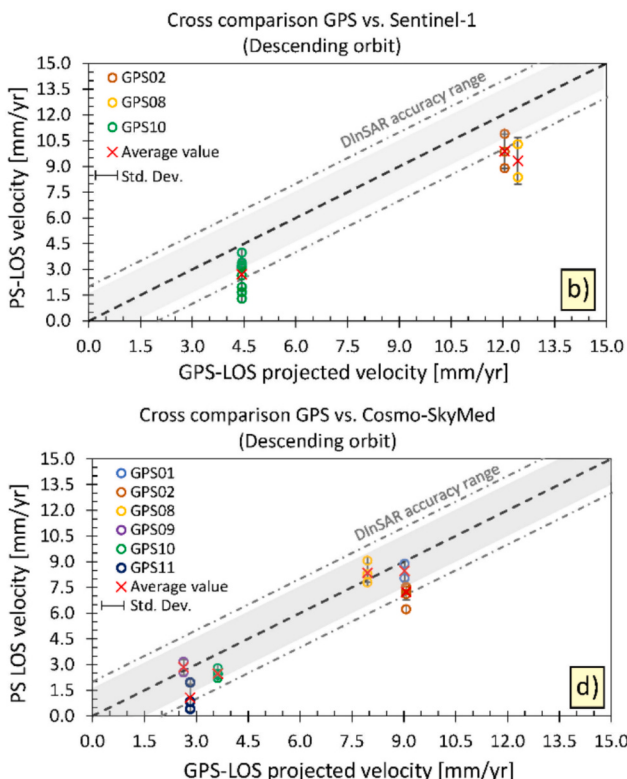
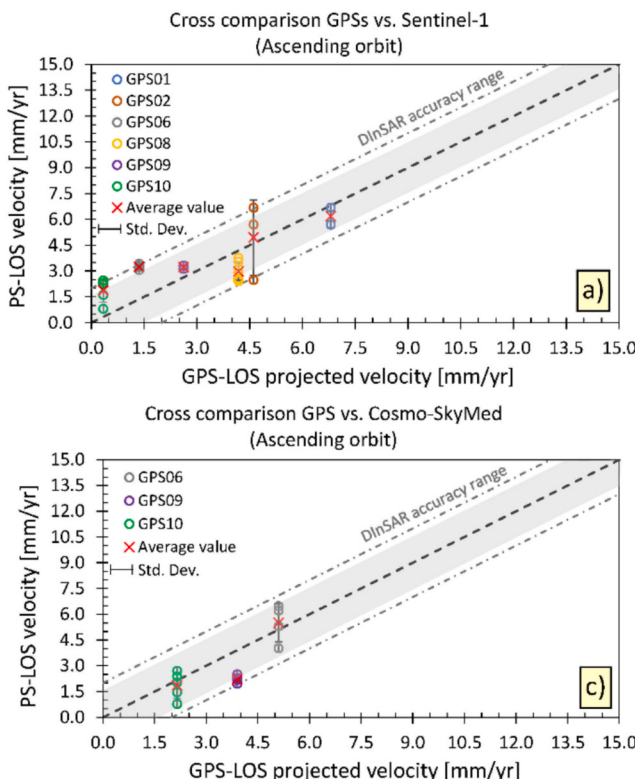


Fig. 10. Cross comparison between the GPS velocity values projected along the reference PS-LOS direction and the PS LOS velocities derived from a) ascending and b) descending Sentinel-1 data and c) ascending and d) descending COSMO-SkyMed data.

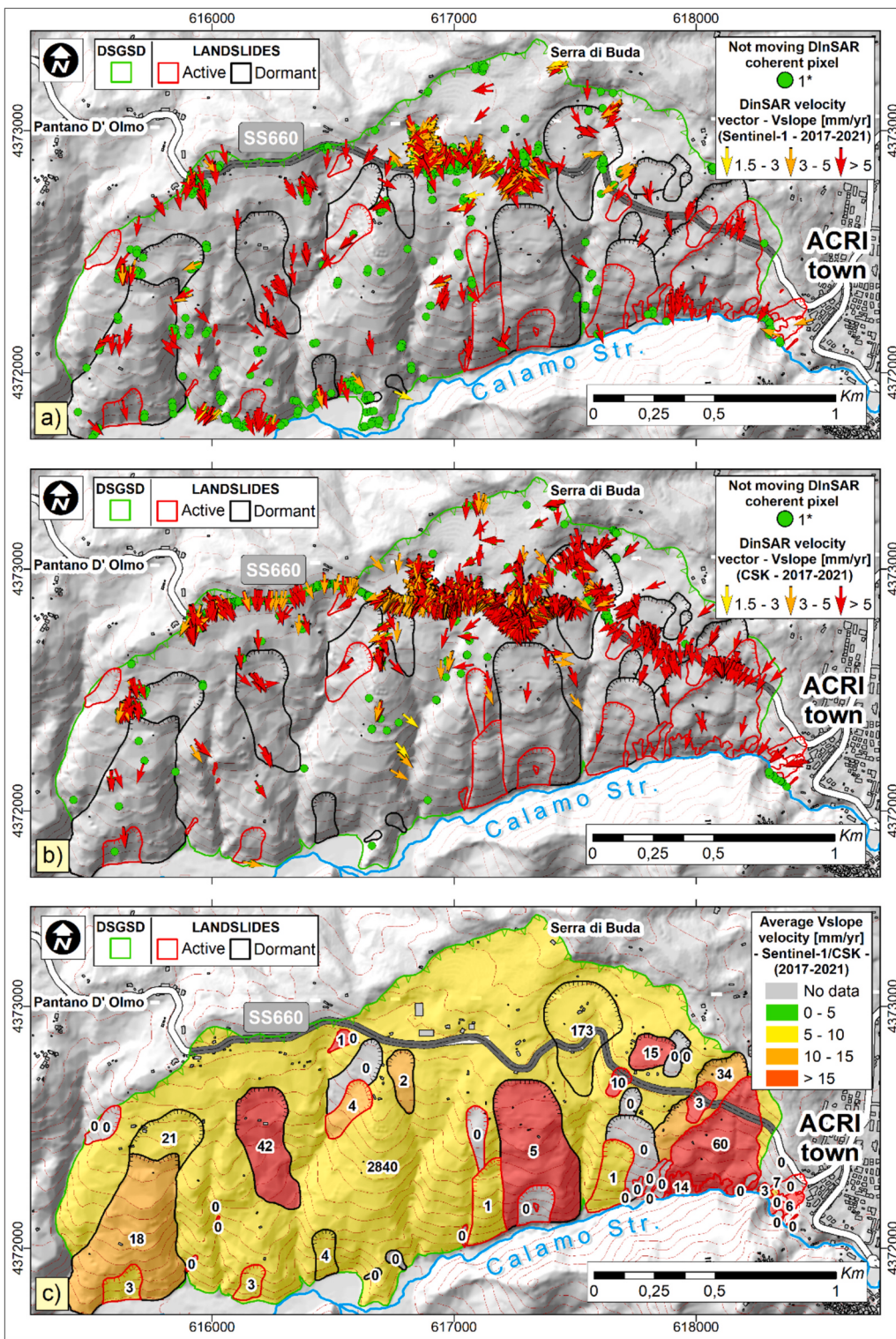


Fig. 11. Maps of projected velocities along the steepest slope direction (V_{slope}) for a) Sentinel-1 and b) CSK MT-DInSAR data (1*: pixel recording a LOS velocity value in the range of -1.5 - 1.5 mm/year corresponding to the MT-DInSAR accuracy and not considered in the projection procedure); c) slow-moving landslides distinguished according to the average $\bar{V}_{slope_landslide}$ velocity by combining Sentinel-1 and CSK/CSG datasets (the number within the landslide body is the number of PSs used to assess the corresponding average \bar{V}_{slope} velocity).

results of the in-situ survey carried out on 14 December 2021, Fig. 13a shows a map and some photos of the SS660 road with 69 damaged sections distinguished according to the severity level recorded to the asphalt pavement. Fig. 13b shows the results of the visual inspections carried out during the same survey on the side retaining structures along

with some photos of the most damaged locations. In particular, the analysed retaining structures are 22: 8 are reinforced concrete walls; 13 are concrete gravity walls; and 1 is an anchored bulkhead (built within the Serra di Buda active rockslide), which was found to be the most damaged work. Indeed, as can be seen in the monographic fact-sheet

Table 4

Key features of typified landslides.

Landslide (ID)	Type	State of activity*	Depth**	Width [m]	Length [m]	Involved geomaterial	$\bar{V}_{slope_landslide}$ [mm/ yr]
1	Slide	MDL	123	314			7.12
2			76	265			—
3			90	251			11.51
4			78	205	Slope debris, colluvial soils, residual soils and gneiss rocks from		—
5			140	150	completely to moderately weathered		—
6			87	153			8.22
7			56	120			32.20
8			65	128			16.12
9	Slide- flow	Active	22	64			—
10	33		37	Detrital-colluvial covers		—	
11	43		75			—	
12	60		45			14.24	
13	31		30			8.92	
14	70		140	Slope debris, colluvial soils, residual soils and gneiss rocks from		17.82	
15	75		150	completely to moderately weathered		—	
16	60		35	Detrital-colluvial covers		—	
17	31		70	Slope debris, colluvial soils, residual soils and gneiss rocks from		—	
18	35		150	completely to moderately weathered		—	
19	28		50	Detrital-colluvial covers		—	
20	230		90			16.04	
21	Slide- flow	Slide	30	150			—
22	MDL		88	Slope debris, colluvial soils, residual soils and gneiss rocks from		15.23	
23	DL		350	completely to moderately weathered		16.02	
24	MDL		108	Gneiss rocks from completely to slightly weathered		8.35	
25	156		285	Slope debris, colluvial soils, residual soils and gneiss rocks from		9.17	
26	9		134	completely to moderately weathered		—	
27	5		20	—		—	
28	10		15	—		—	
29	Slide- flow	Active	SL	6	49	—	—
30	6		62	Detrital-colluvial covers		—	
31	8		19			—	
32	29		86			—	
33	Slide		MDL	12	75		—
34	80		190	Slope debris, colluvial soils, residual soils and gneiss rocks from		5.93	
35	116		304	completely to moderately weathered		—	
36	Slide- flow		97	262	—		10.01
37	49		98	Detrital-colluvial covers		—	
38	30		75			—	
39	137		160			17.10	
40	134		184	Slope debris, colluvial soils, residual soils and gneiss rocks from		—	
41	Slide	Dormant	45	62	completely to moderately weathered		—
42	82		118	—		—	
43	217		380	Gneiss rocks from completely to slightly weathered		12.92	
44	330		522			11.24	
45	315		584			6.15	
46	Slide- flow		216	240			—
47	176		480	Slope debris, colluvial soils, residual soils and gneiss rocks from		18.00	
48	280		465	completely to moderately weathered		7.22	
49	DSGSD	—	217	590	—		18.71
50	5500	1240	Gneiss rocks from completely to slightly weathered		6.93		
51	Slide	Active	16	34			—
52	SL	10	Slope debris, colluvial soils, residual soils and gneiss rocks from		17.82		
53	33	24	completely to moderately weathered		—		
	33	67	—		16.42		

* Note: state of activity based on geomorphological assessments. ** Note: SL: shallow landslide; MDL: medium-deep landslide; DL: deep landslide.

shown in Fig. 8, over time the progressive worsening of its conditions ended up to a partial collapse in 2013, which was still clear during the on-site survey of 14 December 2021. Then, the lengths of the sections (in meters) with uniform levels of damage were identified according to the procedure described in Section 3.2, which accounted for the damage to both the pavement and the side retaining structures. The results are shown in Figs. 14a,b,c, which depict the damage severity levels recorded in November 2008 (Fig. 14a), May 2011 (Fig. 14b), and December 2021 (in this case the results coincided with those of the survey carried out in May 2021 using Google Street View imagery) (Fig. 14c). From the maps it can be ascertained that the conditions of the road surface worsened from November 2008 to May 2011. In particular, the damage mainly

concentrated in the Serra di Buda rockslide due to its reactivation in 2005 and 2010 (Gullà, 2014). In the period 2011–2021, a replacement of the road surface was carried out as revealed by the archive photos systematically acquired by the IRPI-CNR.

Importantly, the analysis of the multi-temporal damage performed on the side retaining structures (whose maps were not reported for brevity) shows that the damage levels associated with the individual works kept constant for a longer time than for the road sections examined. This difference is attributable to the limited frequency of maintenance/replacement works on the retaining works with respect to repairs of the road pavement due to their higher costs. Moreover, in many cases road pavement maintenance works are sufficient to avoid road closure

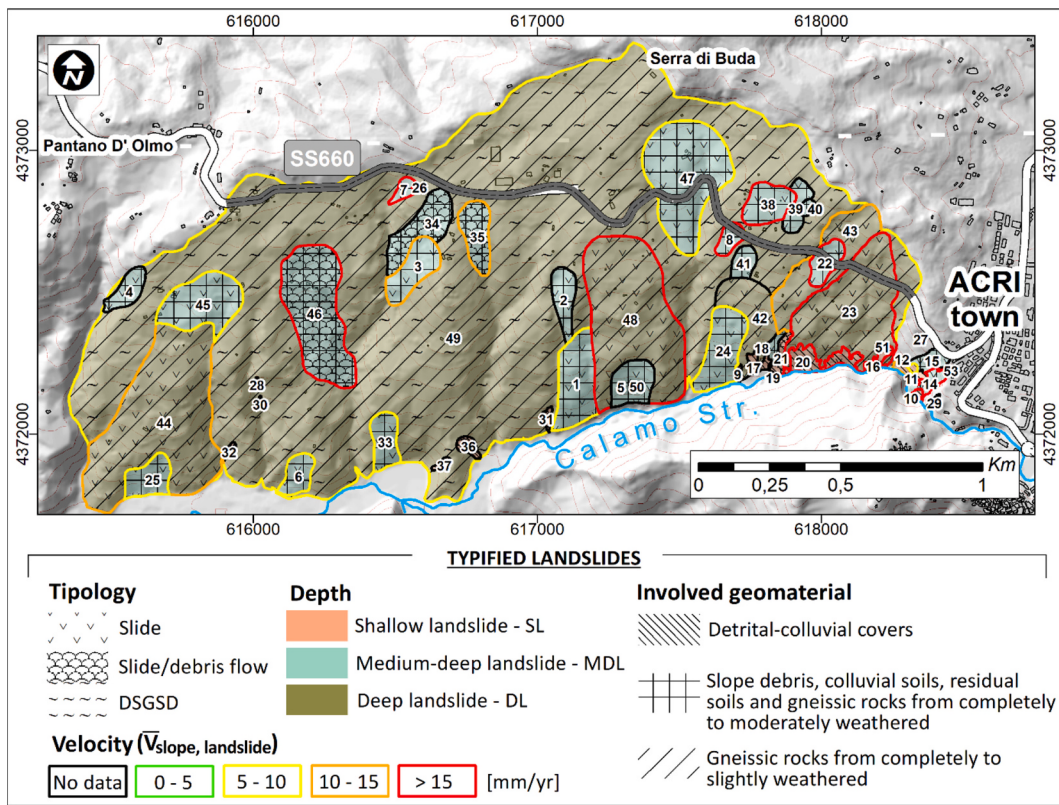


Fig. 12. Map of typified landslides (the number within the landslide body is the landslide ID referred to Table 4).

or traffic reduction.

To deepen this latter aspect, starting from the virtual surveys of Google Street view (November 2008, May 2011, May 2021) available for the 182 m-long stretch crossing the Serra di Buda active rockslide, a detailed analysis of damage evolution was performed by integrating the archive photos relating to the in-situ surveys carried out over the years by the IRPI–CNR with the more recent survey carried out on 14 December 2021.

The association with the four levels of damage severity defined in Section 3.2 allowed deriving the maps shown in Fig. 15 and summarized in the graph below. Both maps and graphs point out that damage levels have increased during the landslide reactivation periods (2004–2005, 2009–2010) that were referred by Gullà (2014).

As a result of both the structural interventions and the replacement of the road surface, in some periods damage severity decreased. Specifically, after the 2005 event, reinforcement works and replacement of the road surface were carried out between March and May 2005. Later, the pavement was reconstructed in June 2013 and replacement and reconstruction operations were carried out between September 2017 and June 2018. Interestingly, the most severe damage was recorded in correspondence of the boundaries of the landslide body (which is mainly translational), being the latter areas of concentration of shear stresses that have affected not only the road surface but also the retaining structures. Indeed, during the recent in-situ survey (dated 14 December 2021) it was possible to verify the good condition of the road pavement located in the central portion (landslide body) following the recent asphalt maintenance carried out in June 2018.

4.3. Phase III

The displacements δ_{slope} (computed according to the procedure described in Section 3.3) within the buffer drawn around each damaged road section (Fig. 16a, b) covered by CSK data (50 road sections out of 69 examined) were cumulated from February 2018 (coinciding with the

last repair works to the road) to December 2021. Both Fig. 16a and c confirm that the highest velocities, and consequently the highest cumulative displacements, occur in the Serra di Buda rockslide and in the adjacent sections.

The computed values of δ_{slope} for each buffer were then associated with the level of damage recorded in the survey of 2021. This allowed retrieving the empirical cause-effect relationship shown in Fig. 17a. As expected, the δ_{slope} attains higher values as the damage severity level (D_i) increases, being D_i conservatively assumed as the most severe damage between the one recorded to the road surface and the pertaining retaining structure (if any). Fig. 17b shows the distribution of the cumulative frequencies representative of the achievement of each level of damage recorded in correspondence of the analysed sections (for damage greater than D0) as a function of δ_{slope} intervals. Starting from the above frequency of occurrence and considering a randomly selected training sample composed by 70 % out of the investigated sections, empirical fragility curves (Fig. 17c) were generated adopting as probabilistic model the log-normal distribution (Eq. 4) and the estimated fragility parameters (Eq. 5 and Eq. 6) pertaining to each D_i ($\beta_i = 0.63, 0.92, 0.51$ and $\bar{\delta}_{slope,i} = 15.46, 26.84, 75.13$ mm for D1, D2 and D3, respectively).

The latter allow evaluating the probability of reaching/exceeding a certain D_i for a fixed value of the δ_{slope} in correspondence of a road section randomly selected among those composing the considered sample. Then, the discrete probabilities provided by the empirical fragility curves were implemented in Eq. (7) to derive the values of the averagely expected damage severity level (μ_D), whose interpolation, through the adoption of the regression model (Eq. 8) with the fitting coefficients equal to $a = 22.0946$, $b = -0.9547$, $c = 0.0101$ and $d = 1.8828$, allowed deriving the empirical vulnerability curve in Fig. 17d.

Finally, the validation of the generated model and the overall accuracy assessment were carried out using the testing (30 % out of the investigated sections) sample via the 3×3 confusion matrix shown in

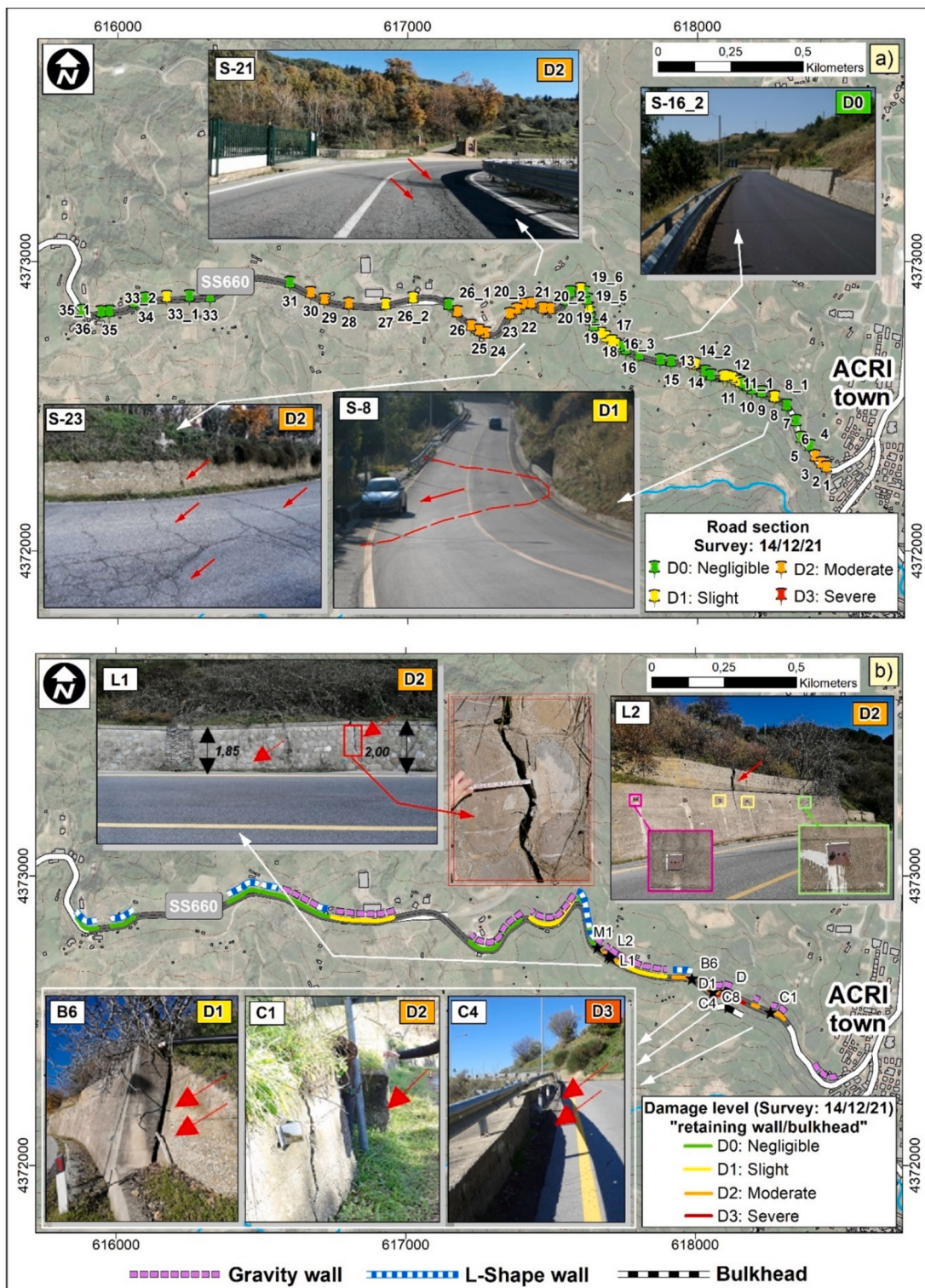


Fig. 13. Some results of the in-situ survey carried out in 14/12/21 to SS660 road: damage ranking to a) the road pavement and b) the side retaining structures.

Fig. 9. In our case its value is equal to 93.3 %; this indicates that the generated model predicts the damage severity level with high accuracy. Furthermore, both sensitivity (95.2 %) and specificity (95.8 %) indicate high ability of the model in correctly identifying positive data out of all true positives classes (sensitivity) and negative data out of all actual negative classes (specificity). Also the precision metric, which provides the quality of positive predictions, is high with a value equal to 95.8 %.

4.4. Phase IV

The expected damage (EDi) for each road section was evaluated at 6 years (2024) starting from 2018, which corresponds to the last repair to the infrastructure (i.e. the road was undamaged) considering three different landslide kinematic scenarios (Fig. 18). In particular, since the investigated landslides over the study area are mainly rainfall-induced with typically seasonal trends and a hydrological response of the

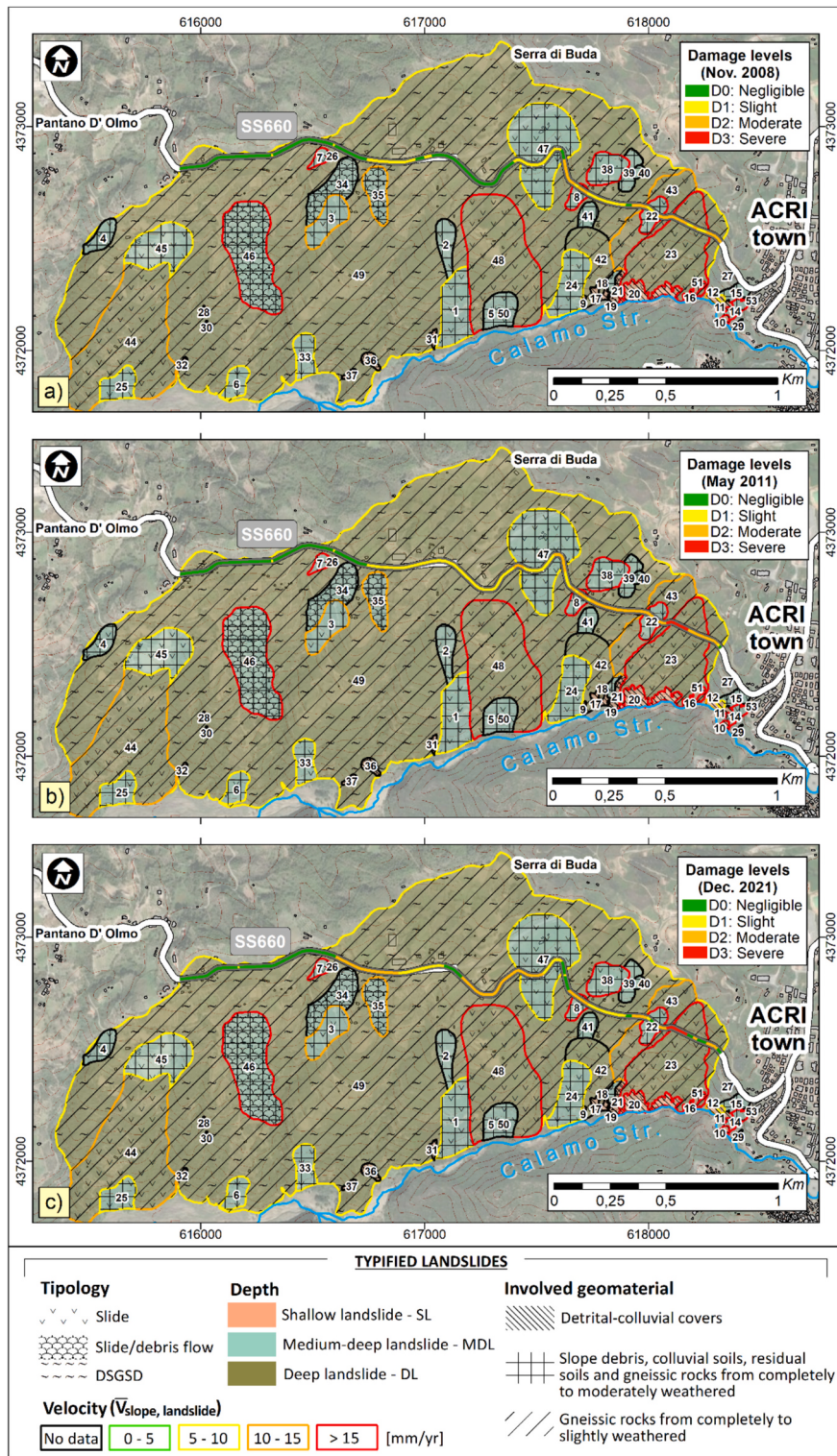


Fig. 14. Integrated multi-temporal damage assessment including road sections and retaining structure interacting with the typified landslides (the number within the landslide body is the landslide ID referred to Table 4): results of the damage classification for a) November 2008 and b) May 2011 virtual surveys, and c) December 2021 field survey.

slopes related to cumulative rainfalls (Gullà, 2014) and considering that relatively dry periods with absence of snow have been recorded over the study area in the recent years, in addition to scenario n. 3, which represents the worst-case with landslides moving with constant V_{slope} values during the time window assumed for the damage forecast on the road stretches, two less severe scenarios with the landslides moving with

slower V_{slope} values were also analysed (scenarios n. 1 and n. 2).

According to these assumptions and adopting the methodology described in Section 3.4 for damage forecast, for the buffer drawn around each damaged section, the δ_{slope} pertaining to each scenario was calculated using Eq. (3) and assuming a constant V_{slope} value derived from the MT-DInSAR data for the first period (2018–2021) and, for the

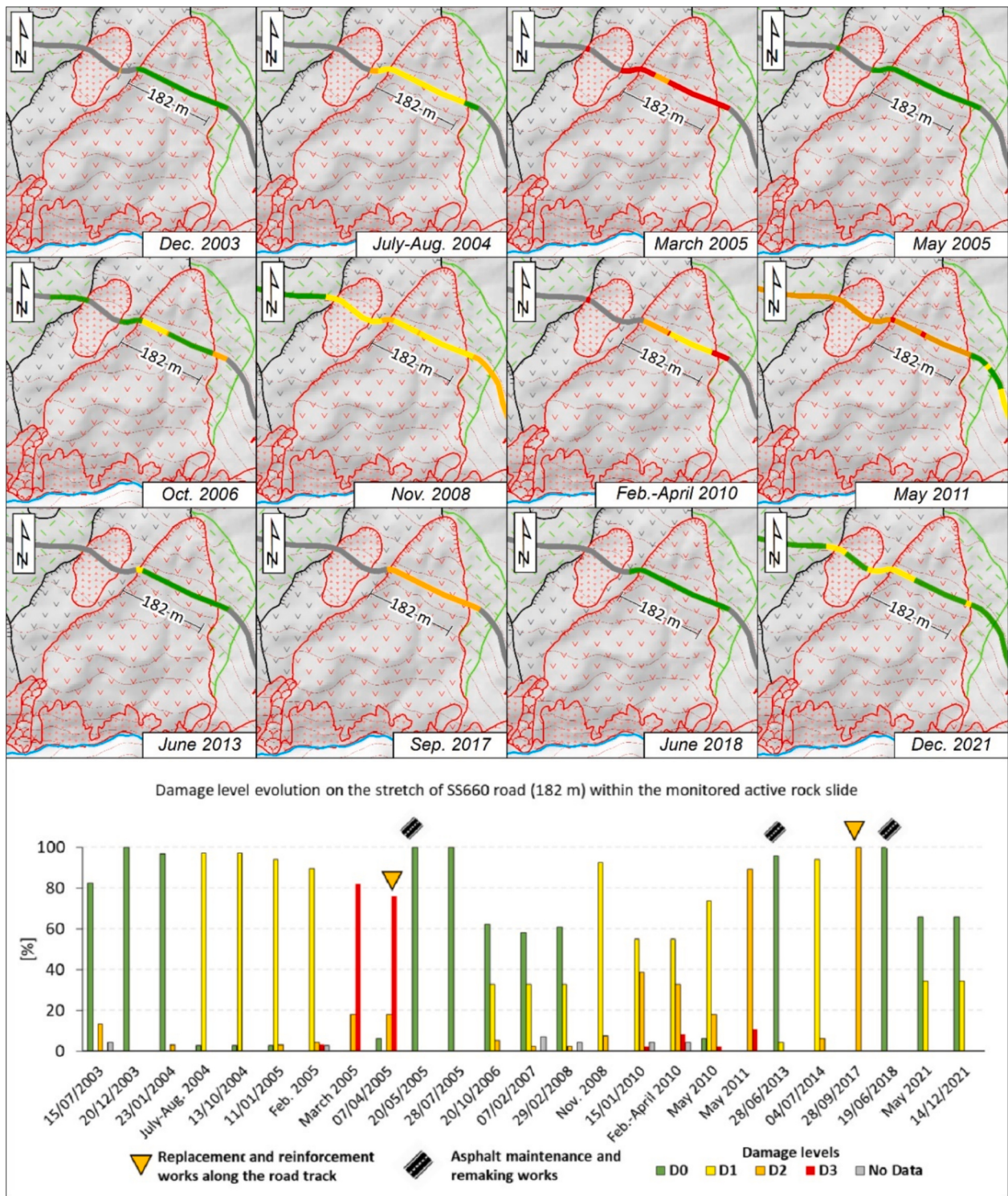


Fig. 15. Temporal evolution of the damage severity levels to the road pavement along 182 m of SS 660 stretch interacting with the monitored active rockslide shown in Fig. 3b. Dates of replacement, reinforcement and asphalt maintenance are shown on the timeline.

second period (i.e. 2021–2024), variable percentages of V_{slope} equal to 25 % (for scenario n. 1), 50 % (for scenario 2) and 100 % (for scenario n. 3).

Subsequently, by entering the vulnerability curve with the δ_{slope} computed for each section in the considered scenario it was possible to derive the averagely expected damage severity level (μ_D) and then, the expected damage (ED_i) based on the numerical index d_i associated with a damage severity level D_i , conservatively assuming the highest D_i level

when the value of μ_D was between two consecutive d_i .

The predicted ED_i associated to each scenario was then extended to the road stretches (damage length, DL) as described in Section 3.4 (see Fig. 18).

Both Fig. 18 and Table 5 highlight that by the end of 2024 the analysed road trunk is expected to have no undamaged sections due to a remarkable worsening of maintenance conditions; indeed, approximately 75 % (for scenario n. 1 – Fig. 18a) and 90 % (for scenarios n. 2

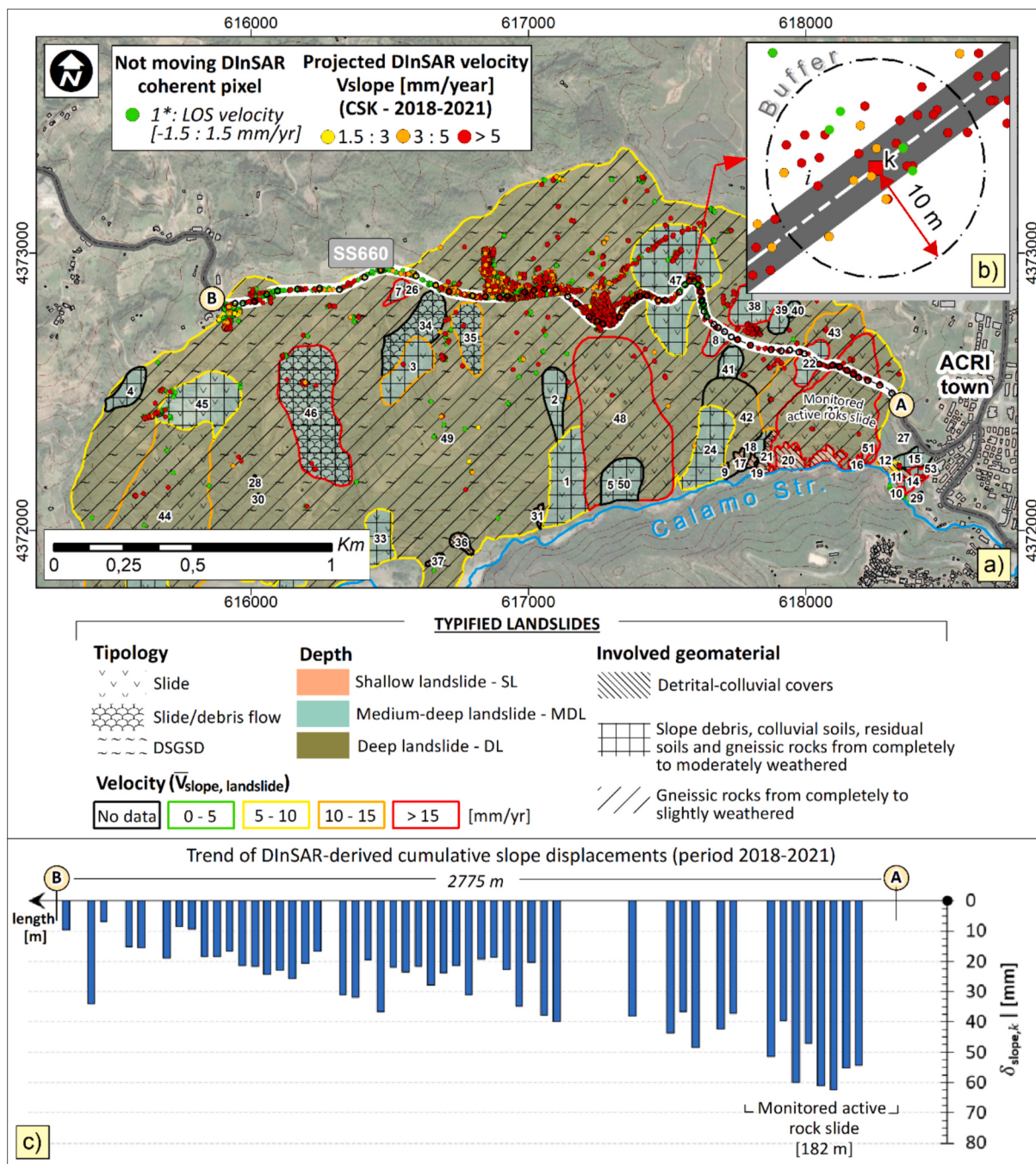


Fig. 16. MT-DInSAR-derived cumulative slope displacements (δ_{slope}) in the period 2018–2021: a) map of projected PSs (COSMO-SkyMed) velocity (V_{slope}) used for the (δ_{slope}) computation along the analysed SS660 (2775 m) in (typified) landslide-affected area (the number within the landslide body is the landslide ID referred to Table 4) with b) close-up view of PSs within 10-m buffer assumed as reference; c) trend of MT-DInSAR-derived cumulative slope displacements (period 2018–2021) along the road track (from point A to point B shown in Fig. 16a).

and n. 3 – Fig. 18b, c) of the road length is expected to exhibit D2-D3 damage levels.

A comparison between the expected damage (EDI) pertaining to each considered scenario with the real damage severity levels, which were detected during a recent field damage survey (carried out in December 2024, i.e. the same reference period assumed for the damage forecast) along the SS660 road stretches (Fig. 18d), shows good match with the scenario n. 1. The performance test was carried out using the 3×3 confusion matrix shown in Fig. 9 by comparing, for each examined road section, the “predicted” damage classes with the “true” damage classes, which were recorded during the survey. Fig. 18 shows that the overall

accuracy as well as the other evaluation metrics such as sensitivity, specificity and precision decrease passing from scenario n. 1 (less severe scenario) to scenario n. 3 (worst-case).

Finally, the quantitative risk (assumed as the expected monetary loss, EML) to the entire road trunk was computed summing the repair costs for all damaged road stretches by using Eq. (10) and considering, for the fixed time scenario (2024), the damage length (DL) and the RUC actualized according to Eq. (9). For this last step the costs of 2021 (see Table 3) were actualized to 2024 by applying a nominal annual interest rate ($r = 2.96\%$) retrieved from the data provided by the Italian Institute for Statistics (ISTAT, 2022) about the yearly change in construction costs

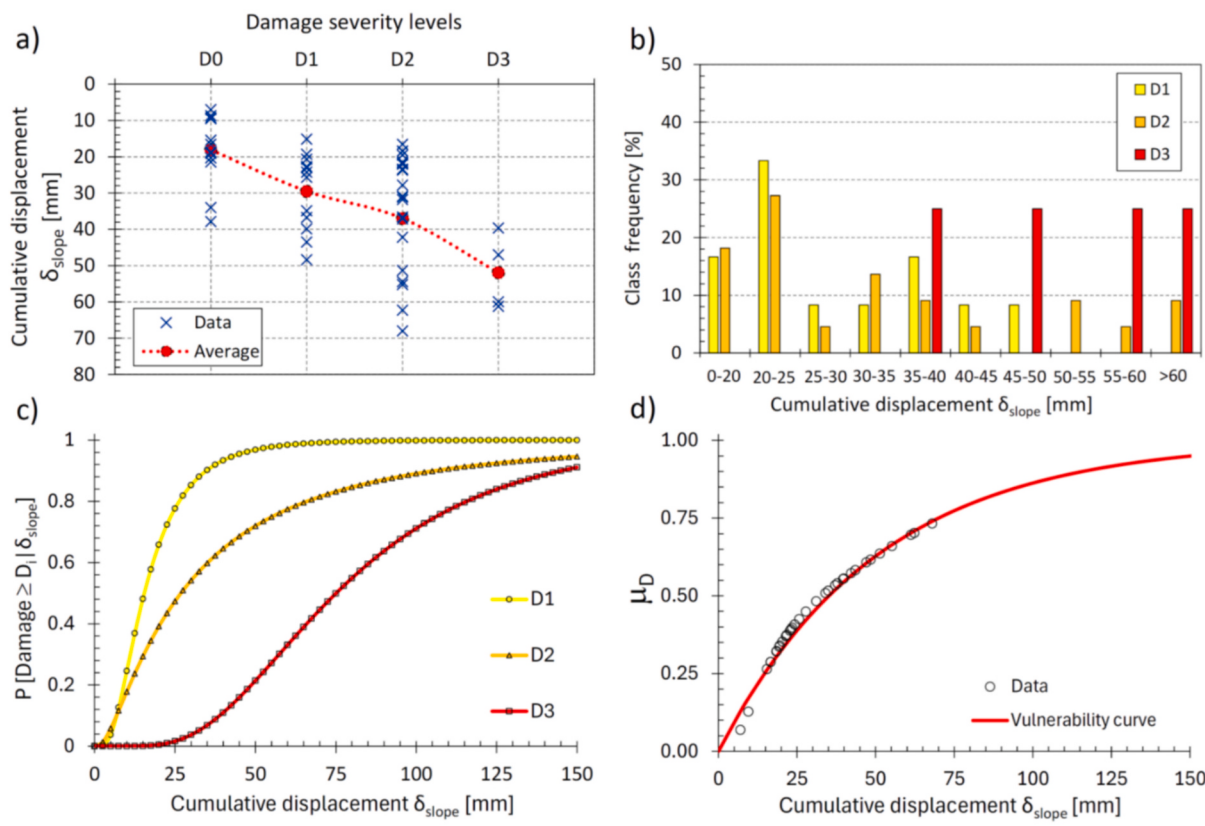


Fig. 17. a) Damage severity level vs. MT-DInSAR-derived cumulative slope displacements (δ_{slope}); b) class frequency of occurrence for each damage level D_i ($i = 1, \dots, 3$); c) empirical fragility curves and d) empirical vulnerability curve (both generated using randomly selected sections corresponding to 70 % out of the total road sections).

of roads over time (from 2015 to 2021) applying a linear regression model. The results in terms of DL and EML for each fixed scenario (n. 1, n. 2 and n. 3) are shown in Table 5 together with a comparison with the repair costs in 2021.

5. Discussion

5.1. Landslide characterization and kinematic feature retrieval

In this work, multi-source data – including conventional geological/geomorphological and geotechnical criteria and widely available remote sensing data – were used to typify the landslides in the study area. This would make it possible exporting the information available for a sample of typified landslides to other landslides in similar geo-environmental contexts where background information is limited. Such kind of procedure could be part of the circular approach proposed by Gullà et al. (2021) that involves (i) the periodical updating of input data as their quality and quantity increase thanks to the results of monitoring and field surveys/investigations, (ii) the use of the knowledge acquired at a given scale to improve the analyses at a smaller scale.

As for MT-DInSAR data, the comparison with GPS data provided an accuracy check that confirmed literature thresholds (Hanssen, 2003; Herrera et al., 2009; Peduto et al., 2018a, 2019) and enabled computing the landslide intensity parameter also where ground-based monitoring data were lacking. Moreover, the limits related to both SAR acquisition geometry and the slope/aspect angles of the area of interest were tackled by projecting SAR data along the steepest slope direction (Cascini et al., 2013) using the threshold from literature that considers the very small sensitivity to North-South components of the ground deformation; this resulted in a limited coverage on those North-South oriented landslides.

As for the use of differential tomography (Fornaro et al., 2014) SAR

image processing in this work, it is worth stressing that, although it is more suitable for linear infrastructure (with limited width) monitoring, it may have limited the PS density in the vegetated landslide-affected areas with respect, for instance, to distributed scatterers (DS-InSAR) approaches. This, however, may have resulted in reduced information on displacements used for landslide typifying rather than the vulnerability and risk analyses (i.e. the main goals of the paper), which, in our study, exploited the data recorded by the PSs located within a buffer with a radius of 10 m drawn around each damaged road section.

Importantly, the study assumed cumulative displacement as the landslide intensity parameter for the vulnerability analysis of the exposed infrastructure; indeed, this parameter allows following the evolution of both the ground displacements and damage severity in certain road sections better than velocity can do, as also pointed out by Picarelli (2011).

5.2. Damage assessment and risk analysis

It is worth stressing that previous studies in literature assess the expected losses or repair costs of roads exposed to landslides by assuming that the roads are undamaged (as an initial condition) and the computation refers to time intervals established in advance (Ferlisi et al., 2021; Zhang et al., 2021). This assumption represents a limit because the roads considered in these analyses already exhibit a damage level that depends on the time since the landslide-induced displacements are cumulating. In the present study, the maintenance state of the analysed road at a time t_0 was known, and the analysis was limited to a following period of 3 years during which the effects of landslide-induced displacements were monitored. This allowed overcoming the uncertainty on the damage severity level at t_0 of the analysis and the typical limit of assuming a constant velocity value for the period of observation, as previous studies

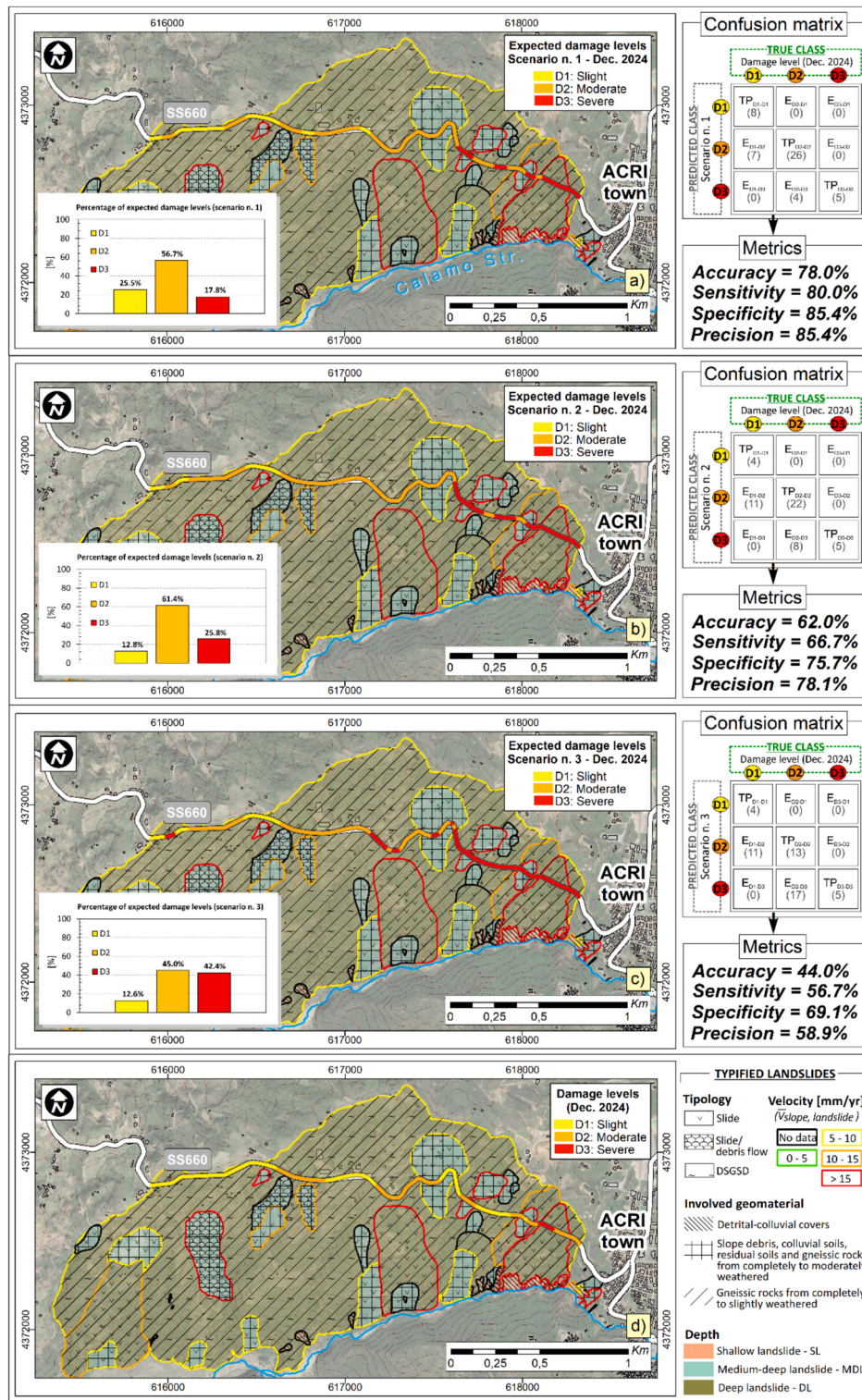


Fig. 18. Maps of the expected damage severity levels affecting the SS 660 road within the Serra di Buda DSGSD in December 2024 (baseline period: 3 years) and damage level percentages for a) scenario n. 1, b) scenario n. 2 and c) scenario n. 3 jointly with the evaluation metrics with reference to the in-situ damage levels recorded in December 2024 as shown in d).

in literature pointed out (Ferlisi et al., 2021; Nappo et al., 2019; Winter et al., 2016).

The combination of Google imagery with archive photos provided a rich background knowledge and represented a cost-effective way to limit the need for in-situ surveys to follow the evolution of road damage. This latter, as a novelty with respect to the existing literature (Mavrouli et al.,

2019; Nappo et al., 2019; Ferlisi et al., 2021), was classified by proposing an original ranking that looked at the road section as a whole including both the pavement and side structures. Indeed, this was particularly crucial in the present study because, in the test area, the side retaining structures are less frequently repaired due to higher costs than partial works, which usually pursue the reopening of the road rather

Table 5

SS660 road damaged length (DL) and expected monetary loss (EML) for each considered scenario (n. 1, n. 2 and n. 3) in December 2024 compared to December 2021.

Damage severity level	DL	EML	DL	EML	DL	EML	DL	EML
	(Dec. 2021)		(Scenario n. 1)		(Scenario n. 2)		(Scenario n. 3)	
	[m]	[€]	[m]	[€]	[m]	[€]	[m]	[€]
D0 road	1492.30	6286.02	—	—	—	—	—	—
D1 road	544.40	22,189.10	709.30	31,550.27	354.33	15,760.80	350.83	15,605.02
D2 road	739.30	88,984.82	1573.20	206,650.38	1705.30	224,002.28	1249.64	164,148.80
D3 road	—	—	493.84	129,378.77	716.71	187,769.22	1175.87	308,062.92
TOT. road	2776.00	117,459.94	2776.00	367,579.42	2776.00	427,532.30	2776.00	487,816.74
D3: Gravity walls	—	—	243.60	61,818.30	243.60	61,818.30	243.60	61,818.30
D3: L-shape walls	—	—	67.877	75,836.11	67.877	75,836.11	67.877	75,836.11
D3: Bulkhead	98.00	410,190.92	98.00	422,332.57	98.00	422,332.57	98.00	422,332.57
TOT. retaining structures	98.00	410,190.92	409.48	559,986.98	409.48	559,986.98	409.48	559,986.98

than acting on the cause(s) of the damage. However, for a period of observation of 3 years, usually no more than one maintenance to the pavement is carried out in the area under consideration. Importantly, for the purpose of the present study the road damage survey dataset (both in-situ and virtual) was analysed with the same procedure (see Section 3.2) and by the same expert in order to limit inherent subjectivity in severity level classification. It is worth stressing that the current geographical coverage of Google Street View could limit the application of this methodology in some countries where these archive images are not available yet (Nappo et al., 2019).

Multi-source multitemporal data allowed deriving fragility and vulnerability curves that tackle the subjectivity in damage classification and other inherent uncertainties concerning the onset and development of damage, which previous works (Peduto et al., 2017; Ferlisi et al., 2021) identified as key limits to this kind of studies. In this regard, it is worth stressing that the exploitation of multi-source remote sensing data (MT-InSAR and Google Street View) allowed gathering an amount of data on displacements and damage, whose collection would have been by far less affordable if derived from conventional in-situ surveys and monitoring.

As for the generated vulnerability curve, the performance test carried out via the confusion matrix revealed an overall accuracy equal to 93.3 %, thus proving that the generated model is capable of predicting the damage severity level in the study area with high accuracy.

With reference to the three analysed kinematic scenarios, the obtained results interestingly showed that, should no countermeasure be taken to mitigate landslide risk, the repair costs to the analysed road stretch (including both the road pavement and the retaining structures) in 2024 would approximately double those of 2021, if the V_{slope} values in the period 2021–2024 are assumed as being the same as in the 2018–2021 period (scenario n. 3, the worst case). Furthermore, DL of the retaining structures in 2024 would almost quadruple with respect to 2021 (independently of the considered scenario), although EML would increase of approximately 30 % because in 2021 the anchored bulkhead, which is the most expensive retaining structure in the study area (see Table 3), already exhibited D3 and was included in EML for 2021. It is worth noting that the best performance of scenario n.1 may be related to the lower cumulated rainfall occurred in the period 2021–2024. Indeed, in these three years, the 120-day values of cumulative rainfall never exceeded the 800 mm threshold that Gullà (2014) associated with the variations in the piezometric levels (approximately 3–6 m) that produce significant changes in the kinematic of Serra di Buda rockslide.

As for repair cost estimation, the discounting cost was assumed to be increasing with a linear trend over the last six years; this represents a weakness that, due to the excessive volatility of costs over the last 2–3 years, may have led to an underestimation of unit costs.

Furthermore, the intangible costs for the community in the event of road disruption and the costs associated with the need to use alternative roads to reach Acri town were not considered, since they are outside the main purpose of this work.

5.3. Exportability of the procedure

Practical challenges might arise when applying the proposed framework in other geo-environmental settings; hereafter they are listed along with strategies to address (if any) possible limitations.

- i) Data availability (e.g. both in-situ and remote sensing data); in this regard, landslide typifying could make the exportation to a similar context less expensive because the exploitation of structured knowledge gathered in a different area supports quantitative landslide risk assessment, thus saving time and economic resources.
- ii) Difference in regional geological-geomorphological-geotechnical features (e.g. landslide types and their kinematics); the procedure to be applied could be similar in the typology of input data and methodological scheme, and the results obtained in a given area could furnish a frame reference to a more efficient landslide risk assessment.
- iii) Rough topography or vegetation that may limit the density of MT-InSAR benchmarks on both landslides and the infrastructure; for this purpose, L-band sensors could be integrated with X- or C-band sensor imagery to achieve an improved data coverage in vegetated areas, also complemented by the installation of corner reflectors on selected benchmarks.
- iv) Maintenance practices (i.e. frequency and type of repair work) related to the typology of the infrastructure and its strategic relevance in terms of traffic management; these differences would limit the exportability of fragility and vulnerability curves to different infrastructures because these tools should be relevant to similar structures in similar geo-environmental contexts to limit data dispersion that is typical of highly heterogeneous samples.
- v) Changes to the procedure could be necessary for its applicability at scales of analysis that are different from the large scale. For instance, the amount and accuracy of input data as well as the parameters used (more or less refined) should be adapted to the level of detail requested by the scale of analysis.

The preceding points – along with issues related to the availability of funding (not immediately quantifiable) needed to address operational costs, dedicated personnel costs, and research and development (R&D) support costs aimed at meeting the maintenance requirements and ensuring continuous updating of input data – affect the sustainability of the proposed procedure. For this purpose, strategies to ensure practical implementation and long-term success of the landslide risk management process should be addressed. For instance, the information gathered on the EML could provide the managing Authorities with practical tools for identifying the road sections on which to intervene as a priority or when the exposed infrastructure reaches unacceptable risk levels. Furthermore, nowadays the exploitation of intelligence technologies provides

useful support to solve key aspects of infrastructure networks, such as design, construction, disaster prevention and mitigation, and rescue and recovery. For instance, digital twin is one of the most promising technologies for multi-stage management that has great potential to address the above challenges for better dealing with such a complex environment (Fuller et al., 2020). Its implementation is currently being promoted in Italy within one of the five National Centers set up by the NRRP (<https://www.supercomputing-icsc.it/en/spoke-5-environment-natura-1-disasters-en/>), which cover certain strategic sectors for the country's development.

6. Conclusions

The paper presented the QRA study for a road interacting with slow-moving landslides of different typologies and exhibiting different kinematic behaviours. When carried out at large scale, this type of study is generally challenging due to the large amount of necessary input data (Ferlisi et al., 2019; Mavrouli et al., 2019; Zhang et al., 2023). Subsequently, relying on conventional approaches mainly based on surveys and ground-based monitoring can be not always affordable in terms of both money and time. This may result in a poor control of the infrastructure by the managing Authority, with the result – apart from the inconvenience to users – of increasing the repair costs and limiting maintenance works only when the road loses its functionality.

The exploitation of multi-source multi-temporal data allowed prioritising different road sections in terms of expected repair costs. The enriched knowledge on the Acri case study was tailored for the analysis of landslide-road interaction and the main results can be recognized as i) the geometric and lithological typifying of landslides; ii) an upgraded road damage ranking, which considers both the condition of the asphalt pavement and the side retaining structures; iii) the damage evolution with respect to the cumulative displacements in between two repair works; iv) empirical fragility and vulnerability curves specifically designed to forecast the economic losses of the infrastructure under study and address countermeasures for landslide risk mitigation in a fixed time scenario.

The integration between the landslide state of activity established on a geomorphological basis and the kinematic characteristics reconstructed by means of Sentinel-1 and COSMO-SkyMed monitoring data emphasises the usefulness of the information gathered from different disciplinary approaches and, in particular, the advisability of updating it periodically in order to create integrated monitoring networks that are sustainable in the medium to long term when dealing with planning and managing roads affected by landslides. Indeed, considering the intrinsic difficulties and (sustainable) costs in defining reliable geotechnical-structural models in analyses aimed at forecasting the real road behavior, the setting up of empirical relationships allows a quick overview of the complex interaction of the infrastructure with unstable slopes. Finally, the combination of MT-DInSAR with conventional ground-based data (i.e. inclinometers, GPS, total stations), multi-temporal damage datasets and fragility/vulnerability curves can help implementing digital twins that, once setup, support informed geotechnical/structural analyses for road resilience assessment. Such tools, used with a circular approach, could reduce the cost of road management and help risk prevention practise even in inner hilly and mountain areas, thus avoiding abandonment that, in turn, typically increases landslide risk.

CRediT authorship contribution statement

D. Peduto: Writing – review & editing, Writing – original draft, Supervision, Methodology, Funding acquisition, Conceptualization. **G. Nicodemo:** Writing – review & editing, Writing – original draft, Methodology, Data curation, Conceptualization. **D. Luongo:** Writing – original draft, Formal analysis, Data curation. **L. Borrelli:** Writing – review & editing, Investigation. **D. Reale:** Software, Data curation. **S. Ferlisi:**

Writing – review & editing. **G. Fornaro:** Funding acquisition, Supervision. **G. Gullà:** Writing – review & editing, Supervision.

Declaration of competing interest

The authors declare the following financial interests/personal relationships which may be considered as potential competing interests:

All Co-authors reports Co-financial support was provided by Italian Space Agency (ASI) with contract n. 2021-10-U.0 CUP F65F21000630005 MEFISTO. If there are other authors, they declare that they have no known competing financial interests or personal relationships that could have appeared to influence the work reported in this paper.

Acknowledgements

This research was funded by and carried out in the Italian Space Agency (ASI) contract n. 2021-10-U.0 CUP F65F21000630005 MEFISTO—*Metodi di Elaborazione di dati SAR multi-Frequenza per il monitoraggio del dissesto idrogeologico—Multi-frequency SAR data processing methods for the hydrogeological instability monitoring*.

The activities also fall within the Agreement for scientific cooperation signed by the Italian National Research Council (CNR-IRPI) and the Department of Civil Engineering of the University of Salerno on “*Attività di ricerca mirate ad approfondire le conoscenze sulla tipizzazione di movimenti franosi a cinematica lenta e sulla vulnerabilità di strutture e infrastrutture che con essi interagiscono anche mediante l'impiego di tecniche innovative di monitoraggio satellitare e da terra*” and the operative Agreement for Research contribution signed by the two institutions on the topic: “*Analisi quantitativa del rischio da frane a cinematica lenta in aree urbane dell'Appennino Meridionale con l'ausilio di modellazione numerica avanzata e dati di monitoraggio satellitare*”.

Appendix A. Supplementary data

Supplementary data to this article can be found online at <https://doi.org/10.1016/j.enggeo.2025.108011>.

Data availability

The dataset generated during and/or analysed during the current study are available from the corresponding author on reasonable request.

References

- Antronico, L., Borrelli, L., Peduto, D., Fornaro, G., Gullà, G., Paglia, L., Zeni, G., 2013. Conventional and innovative techniques for the monitoring of displacements in landslide affected area. In: Margottini, C., Canuti, P., Sassa, K. (Eds.), Landslide Science and Practice—Early Warning, Instrumentation and Monitoring, Springer—vol. vol. 2, pp. 125–131. <https://doi.org/10.1007/978-3-642-31445-2>.
- Borrelli, L., Gullà, G., 2017. Tectonic constraints on a deep-seated rock slide in weathered crystalline rocks. *Geomorphology* 290, 288–316. <https://doi.org/10.1016/j.geomorph.2017.04.025>.
- Borrelli, L., Greco, R., Gullà, G., 2007. Weathering grade of rock masses as a predisposing factor to slope instabilities: Reconnaissance and control procedures. *Geomorphology* 87 (3), 158–175. <https://doi.org/10.1016/j.geomorph.2006.03.031>.
- Borrelli, L., Antronico, L., Gullà, G., Sorriso-Valvo, G.M., 2014a. Geology, geomorphology and dynamics of the 15 February 2010 Maierato landslide (Calabria, Italy). *Geomorphology* 208, 50–73. <https://doi.org/10.1016/j.geomorph.2013.11.015>.
- Borrelli, L., Perri, F., Critelli, S., Gullà, G., 2014b. Characterization of granitoid and gneissic weathering profiles of the Mucone River basin (Calabria, southern Italy). *Catena* 113, 325–340. <https://doi.org/10.1016/j.catena.2013.08.014>.
- Caleca, F., Tofani, V., Segoni, S., Raspini, F., Rosi, A., Natali, M., Catani, F., Casagli, N., 2022. A methodological approach of QRA for slow-moving landslides at a regional scale. *Landslides* 19, 1539–1561. <https://doi.org/10.1007/s10346-022-01875-x>.
- Cascini, L., Gullà, G., 1993. Caratterizzazione fisico-mecanica dei terreni prodotti dall'alterazione di rocce gneissiche. *Rivista Italiana di Geotecnica*, Anno XXVII, N. 2, Aprile-Giugno 1993, 125–147 (in Italian).

- Cascini, L., Fornaro, G., Peduto, D., 2010. Advanced low- and full-resolution DInSAR map generation for slow-moving landslide analysis at different scales. Eng. Geol. 112 (1–4), 29–42. <https://doi.org/10.1016/j.engevo.2010.01.003>.
- Cascini, L., Peduto, D., Pisciotta, G., Arena, L., Ferlisi, S., Fornaro, G., 2013. The combination of DInSAR and facility damage data for the updating of slow-moving landslide inventory maps at medium scale. Nat. Hazards Earth Syst. Sci. 13, 1527–1549. <https://doi.org/10.5194/nhess-13-1527-2013>.
- Cignetti, M., Godone, D., Notti, D., Zucca, F., Meisina, C., Bordoni, M., Pedretti, L., Lanteri, L., Bertolo, D., Giordan, D., 2023. Damage to anthropic elements estimation due to large slope instabilities through multi-temporal A-DInSAR analysis. Nat. Hazards 115, 2603–2632. <https://doi.org/10.1007/s11069-022-05657-7>.
- Colesanti, C., Wasowski, J., 2006. Investigating landslides with space-borne Synthetic Aperture Radar (SAR) interferometry. Eng. Geol. 88, 173–199. <https://doi.org/10.1016/j.engevo.2006.09.013>.
- Corominas, J., van Westen, C., Frattini, P., Cascini, L., Malet, J.-P., Fotopoulos, S., Catani, F., Van Den Eeckhout, M., Mavrouli, O., Agliardi, F., Pitilakis, K., Winter, M. G., Pastor, F.S., Tofani, V., Hervás, J., Smith, J.T., 2014. Recommendations for the quantitative analysis of landslide risk. Bull. Eng. Geol. Environ. 73, 209–263. <https://doi.org/10.1007/s10064-013-0538-8>.
- Dei Cas, L., Trigila, A., Iadanza, C., 2021. Linee Guida per il monitoraggio delle frane. In: Linee Guida SNPA 32/2021, pp. 228, ISBN: 978-88-448-1071-9, (in Italian). https://www.snpambiente.it/wp-content/uploads/2021/09/Linee_Guida_SN_PA_Monitoraggio_frane_web.pdf.
- Domenichini, L., Di Mascio, P., Giannattasio, P., Caliendo, C., Festa, B., Marchionna, A., Finni, P., Molinaro, E., Paoloni, G., 1993. Modello di catalogo delle pavimentazioni stradali. In: Fondazione Politecnica per il Mezzogiorno d'Italia, Naples, pp. 44 (in Italian).
- Donnini, M., Napolitano, E., Salvati, P., Ardizzone, F., Bucci, F., Fiorucci, F., Santangelo, M., Cardinali, M., Guzzetti, F., 2017. Impact of event landslides on road networks: a statistical analysis of two Italian case studies. Landslides 14, 1521–1535. <https://doi.org/10.1007/s10346-017-0829-4>.
- Fan, Q., Zhang, S., Niu, Y., Zeng, X., Si, J., Li, X., Wu, W., Jiang, J., Qiu, S., Kang, Y., 2024. A non-contact quantitative risk assessment framework for translational highway landslides: Integration of InSAR, geophysical inversion, and numerical simulation. Eng. Geol. 107818. <https://doi.org/10.1016/j.engevo.2024.107818>.
- Fell, R., Corominas, J., Bonnard, C., Cascini, L., Leroy, E., Savage, W.Z., 2008. Guidelines for landslide susceptibility, hazard and risk zoning for land use planning. Eng. Geol. 102, 85–98. <https://doi.org/10.1016/j.engevo.2008.03.022>.
- Ferlisi, S., De Chiara, G., 2016. Risk analysis for rainfall-induced slope instabilities in coarse-grained soils: practice and perspectives in Italy. In: Aversa, S., Cascini, L., Picarelli, L., Scavia, C. (Eds.), Landslides and Engineered Slopes. Experience, Theory and Practice. Proc. of the 12th International Symposium on Landslides, Naples (Italy), 12–19 June 2016, 1. CRC Press/Balkema, Taylor & Francis Group, Leiden (The Netherlands), pp. 137–154.
- Ferlisi, S., De Chiara, G., Cascini, L., 2016. Quantitative risk analysis for hyperconcentrated flows in Nocera Inferiore (southern Italy). Nat. Hazards 81 (Supplement 1), S89–S115. <https://doi.org/10.1007/s11069-015-1784-9>.
- Ferlisi, S., Gullà, G., Nicodemo, G., Peduto, D., 2019. A multi-scale methodological approach for slow-moving landslide risk mitigation in urban areas, southern Italy. Euro-Mediterr. J. Environ. Integr. 4, 20. <https://doi.org/10.1007/s41207-019-0110-4>.
- Ferlisi, S., Marchese, A., Peduto, D., 2021. Quantitative analysis of the risk to road networks exposed to slow-moving landslides: a case study in the Campania region (southern Italy). Landslides 18, 303–319. <https://doi.org/10.1007/s10346-020-01482-8>.
- Fornaro, G., Pauciullo, A., Serafino, F., 2009. Deformation monitoring over large areas with multipass differential SAR interferometry: a new approach based on the use of spatial differences. Int. J. Remote Sens. 30 (6), 1455–1478. <https://doi.org/10.1080/01431160802459569>.
- Fornaro, G., Verde, S., Reale, D., Pauciullo, A., 2014. CAESAR: an approach based on covariance matrix decomposition to improve multibaseline–multitemporal interferometric SAR processing. IEEE Trans. Geosci. Remote Sens. 53 (4), 2050–2065. <https://doi.org/10.1109/TGRS.2014.2352853>.
- Fotopoulos, S.D., Pitilakis, K.D., 2013. Vulnerability assessment of reinforced concrete buildings subjected to seismically triggered slow-moving earth slides. Landslides 10 (5), 563–582. <https://doi.org/10.1007/s10346-012-0345-5>.
- Frattini, P., Crosta, G.B., Rossini, M., Allievi, J., 2018. Activity and kinematic behaviour of deep-seated landslides from PS-InSAR displacement rate measurements. Landslides 15 (6), 1053–1070. <https://doi.org/10.1007/s10346-017-0940-6>.
- Fuller, A., Fan, Z., Day, C., Barlow, C., 2020. Digital twin: enabling technologies, challenges and open research. IEEE Access 8, 108952–108971. <https://doi.org/10.1109/ACCESS.2020.2998358>.
- Galli, M., Guzzetti, F., 2007. Landslide vulnerability criteria: a case study from Umbria, Central Italy. Environ. Manag. 40, 649–665. <https://doi.org/10.1007/s00267-006-0325-4>.
- Gullà, G., 2014. Field monitoring in sample sites: hydrological response of slopes with reference to widespread landslide events. Proc. Earth Planet. Sci. 9 (2014), 44–53.
- Gullà, G., Aceto, L., Perna, E., 2003. Caratterizzazione geotecnica dei terreni di alterazione e/o degradazione di Acri. CNR-IRPI Internal Report 614, 1–115 (In Italian).
- Gullà, G., Aceto, L., Antronico, L., Cilento, M., Niciforo, D., Perna, E., Terranova, O., 2004a. Failure and post failure conditions of a landslide involving weathered and degraded rocks. In: Proc. of the 9th International Symposium on Landslides, Rio de Janeiro, June 28 - July 7, 2004, pp. 1241–1246.
- Gullà, G., Niciforo, D., Bonci, L., Calcaterra, S., Cesi, C., Gambino, P., 2004b. Surface movements of a landslide involving weathered and degraded rocks. In: Proc. of the 15th Southeast Asian Geotechnical Conference (15th SEAGC), Bangkok, November 22–26, 2004, 1, pp. 375–378.
- Gullà, G., Caloiero, T., Coccarelli, R., Petrucci, O., 2012. A proposal for a methodological approach to the characterization of Widespread Landslide Events: an application to Southern Italy. Nat. Hazards Earth Syst. Sci. 12, 165–173. <https://doi.org/10.5194/nhess-12-165-2012>.
- Gullà, G., Peduto, D., Borrelli, L., Antronico, L., Fornaro, G., 2017. Geometric and kinematic characterization of landslides affecting urban areas: the Lungro case study (Calabria, Southern Italy). Landslides 14 (1), 171–188. <https://doi.org/10.1007/s10346-015-0676-0>.
- Gullà, G., Borrelli, L., Aceto, L., 2020. Frane tipizzate in rocce gneissiche: rilevanza e stato dell'arte. In: Atti della XII Edizione "Tecniche per la Difesa del Suolo e dall'Inquinamento", Volume 41, 213–227 - 2020. A cura di Giuseppe Frega & Francesco Macchione. EdiBios. ISBN: 978-88-97181-75-0 - ISSN 2282-5517.
- Gullà, G., Nicodemo, G., Ferlisi, S., Borrelli, L., Peduto, D., 2021. Small-scale analysis to rank municipalities requiring slow-moving landslide risk mitigation measures: the case study of the Calabria region (southern Italy). Geoenviron. Disasters 8, 31. <https://doi.org/10.1186/s40677-021-00202-1>.
- Hanssen, F.R., 2003. Subsidence monitoring using contiguous and PSInSAR: quality assessment based on precision and reliability. In: Proc. 11th FIG Symposium on Deformation Measurements, Santorini, Greece, pp. 1–8.
- Herrera, G., Fernandez-Merodo, J., Tomas, R., Cooksley, G., Mulas, J., 2009. Advanced interpretation of subsidence in Murcia (SE Spain) using A-DInSAR data-modelling and validation. Nat. Hazard. Earth Syst. Sci. 9, 647–661.
- Herrera, G., Gutierrez, F., Garcia-Davalillo, J.C., Guerrero, J., Notti, D., Galve, J.P., Fernandez-Merodo, J.A., Cooksley, G., 2013. Multi-sensor advanced DInSAR monitoring of very slow landslides: the Tena Valley case study (Central Spanish Pyrenees). Remote Sens. Environ. 128, 31–43. <https://doi.org/10.1016/j.rse.2012.09.020>.
- Infante, D., Di Martire, D., Calcaterra, D., Miele, P., Scotto di Santolo, A., Ramondini, M., 2019. Integrated procedure for monitoring and assessment of linear infrastructures safety (I-Pro MONALISA) affected by slope instability. Appl. Sci. 9 (24), 5535. <https://doi.org/10.3390/app9245535>.
- ISTAT, 2022. http://dati.istat.it/Index.aspx?DataSetCode=DCSC_FABBRESID_1. Accessed (last access: 30 December 2023).
- Journalt, J., Macciotta, R., Hendry, M.T., Charbonneau, F., Huntley, D., Bobrowsky, P.T., 2018. Measuring displacements of the Thompson River valley landslides, south of Ashcroft, BC, Canada, using satellite InSAR. Landslides 15 (4), 621–636. <https://doi.org/10.1007/s10346-017-0900-1>.
- Lu, P., Catani, F., Tofani, V., Casagli, N., 2014. Quantitative hazard and risk assessment for slow-moving landslides from persistent scatterer interferometry. Landslides 11 (4), 685–696. <https://doi.org/10.1007/s10346-013-0432-2>.
- Luo, H.Y., Zhang, L.M., Zhang, L.L., He, J., Yin, K.S., 2023. Vulnerability of buildings to landslides: the state of the art and future needs. Earth Sci. Rev. 238, 104329. <https://doi.org/10.1016/j.earscirev.2023.104329>.
- Mansour, M.F., Morgenstern, N.R., Martin, C.D., 2011. Expected damage from displacement of slow-moving slides. Landslides 8 (1), 117–131. <https://doi.org/10.1007/s10346-010-0227-7>.
- Mavrouli, O., Corominas, J., Ibarbia, I., Nahikari Alonso, N., Ioseba Jugo, I., Ruiz, J., Lutzuraga, S., Navarro, J.A., 2019. Integrated risk assessment due to slope instabilities in the roadway network of Gipuzkoa, Basque Country. Nat. Hazards Earth Syst. Sci. 19 (2), 399–419. <https://doi.org/10.5194/nhess-19-399-2019>.
- Nappo, N., Peduto, D., Mavrouli, O., van Westen, C.J., Gullà, G., 2019. Slow-moving landslides interacting with the road network: analysis of damage using ancillary data, in situ surveys and multi-source monitoring data. Eng. Geol. 260, 105244. <https://doi.org/10.1016/j.engevo.2019.105244>.
- Nappo, N., Mavrouli, O., Nex, F., van Westen, C., Gambillara, R., Michetti, A.M., 2021. Use of UAV-based photogrammetry products for semi-automatic detection and classification of asphalt road damage in landslide-affected areas. Eng. Geol. 294, 106363. <https://doi.org/10.1016/j.engevo.2021.106363>.
- Negulescu, C., Ulrich, A., Seyed, D.M., 2014. Fragility curves for masonry structures submitted to permanent ground displacements and earthquakes. Nat. Hazards 74, 1461–1474. <https://doi.org/10.1007/s11069-014-1253-x>.
- Nicodemo, G., Peduto, D., Ferlisi, S., Gullà, G., Reale, D., Fornaro, G., 2018. DInSAR data integration in vulnerability analysis of buildings exposed to slow-moving landslides. In: Proceedings of IEEE International Geoscience and Remote Sensing Symposium (IGARSS 2018), Valencia (Spain), 22–27 July, 2018, pp. 6111–6114. <https://doi.org/10.1109/IGARSS.2018.8518808>.
- Nicodemo, G., Peduto, D., Korff, M., Ferlisi, S., 2020. Multi-parameter probabilistic vulnerability analysis of settlement-affected masonry buildings with shallow/piled foundations in soft soils: case studies in The Netherlands. In: Calvet, F., et al. (Eds.), Proceedings of the VII Italian Conference of Researchers in Geotechnical Engineering – CNRIG – Lecco, Italy 3–5 July, 2019, vol. 40. © Springer Nature Switzerland AG 2020, LNCE, pp. 42–51. https://doi.org/10.1007/978-3-030-21359-6_5.
- North, M., Farewell, T., Hallet, S., Bertelle, A., 2017. Monitoring the response of roads and railways to seasonal soil movement with persistent scatterers interferometry over six UK sites. Remote Sens. (Basel) 9, 1–17. <https://doi.org/10.3390/rs9090922>.
- Noviello, C., Verde, S., Zamparella, V., Fornaro, G., Pauciullo, A., Reale, D., Nicodemo, G., Ferlisi, S., Gullà, G., Peduto, D., 2020. Monitoring buildings at landslide risk with SAR: a methodology based on the use of multipass interferometric data. IEEE Geosci. Remote Sensing Mag. 8 (1), 91–119. <https://doi.org/10.1109/MGRS.2019.2963140>.
- Pecoraro, G., Nicodemo, G., Menichini, R., Luongo, D., Peduto, D., Calvello, M., 2023. Combining statistical, displacement and damage analyses to study slow-moving landslides interacting with roads: two case studies in southern Italy. Appl. Sci. 13 (5), 3368. <https://doi.org/10.3390/app13053368>.

- Peduto, D., Ferlisi, S., Nicodemo, G., Reale, D., Pisciotta, G., Gullà, G., 2017. Empirical fragility and vulnerability curves for buildings exposed to slow-moving landslides at medium and large scales. *Landslides* 14 (6), 1993–2007. <https://doi.org/10.1007/s10346-017-0826-7>.
- Peduto, D., Elia, F., Montuori, R., 2018a. Probabilistic analysis of settlement-induced damage to bridges in the city of Amsterdam (the Netherlands). *Transport. Geotech.* 14, 169–182. <https://doi.org/10.1016/j.trgeo.2018.01.002>.
- Peduto, D., Nicodemo, G., Carraffa, M., Gullà, G., 2018b. Quantitative analysis of consequences induced by slow-moving landslides to masonry buildings: a case study. *Landslides* 15 (10), 2017–2030. <https://doi.org/10.1007/s10346-018-1014-0>.
- Peduto, D., Korff, M., Nicodemo, G., Marchese, A., Ferlisi, S., 2019. Empirical fragility curves for settlement-affected buildings: analysis of different intensity parameters for seven hundred masonry buildings in the Netherlands. *Soils Found.* 59 (2), 380–397. <https://doi.org/10.1016/j.sandf.2018.12.009>.
- Peduto, D., Santoro, M., Aceto, L., Borrelli, L., Gullà, G., 2021. Full integration of geomorphological, geotechnical, A-DInSAR and damage data for detailed geometric-kinematic features of a slow-moving landslide in urban area. *Landslides* 18, 807–825. <https://doi.org/10.1007/s10346-020-01541-0>.
- Picarelli, L., 2011. Discussion to the paper “Expected damage from displacement of slow-moving slides” by MF Mansour, NR Morgenstern and CD Martin. *Landslides* 8 (4), 553–555. <https://doi.org/10.1007/s10346-011-0292-6>.
- Pitilakis, K.D., Fotopoulou, S.D., 2015. Vulnerability assessment of buildings exposed to coseismic permanent slope displacements. In: Winter, M.G., Smith, D.M., Eldred, P.J. L., Toll, D.G. (Eds.), *Geotechnical Engineering for Infrastructure and Development*. ICE Publishing, pp. 151–173. <https://doi.org/10.1680/ecsmge.60678>.
- Plank, S., Singer, J., Minet, Ch., Thuro, K., 2010. GIS based suitability evaluation of the differential radar interferometry method (DInSAR) for detection and deformation monitoring of landslides. In: Lacoste-Francis, H. (Ed.), *Proc. Fringe 2009 Workshop*, 30 November–4 December 2009, ESRIN, Frascati, Italy (ESA SP-677), 8 pp., ISBN: 978-92-9221-41-4, 2010.
- Prezzario Regionale OO.PP. Calabria, 2021. <https://www.regione.calabria.it/website/organizzazione/dipartimento6/subsite/lavoripubblici/prezzariօoopp/> Accessed (last access: 30 November 2023).
- Reinders, K.J., Giardina, G., Zurfluh, F., Ryser, J., Hanssen, R.F., 2022. Proving compliance of satellite InSAR technology with geotechnical design codes. *Transport. Geotech.* 33, 100722. <https://doi.org/10.1016/j.trgeo.2022.100722>.
- Reyes-Carmona, C., Barra, A., Galve, J.P., Monserrat, O., Pérez-Peña, J.V., Mateos, R.M., Notti, D., Ruano, P., Millares, A., López-Vinieles, J., Azanón, J.M., 2020. Sentinel-1 DInSAR for monitoring active landslides in critical infrastructures: the case of the rules reservoir (southern Spain). *Remote Sens. (Basel)* 12 (5), 809. <https://doi.org/10.3390/rs12050809>.
- Sharp, R.W., Booker, J.R., 1984. Shakedown of pavements under moving surface loads. *J. Transp. Eng.* 110 (1). [https://doi.org/10.1061/\(ASCE\)0733-947X\(1984\)110:1\(1\)](https://doi.org/10.1061/(ASCE)0733-947X(1984)110:1(1)).
- Shinozuka, M., Feng, M.Q., Kim, H.K., Uzawa, T., Ueda, T., 2003. Statistical Analysis of Fragility Curves. Technical report MCEEER-03-0002. State University of New York, Buffalo, p. 173. <https://www.eng.buffalo.edu/mceer-reports/03/03-0002.pdf>.
- Terranova, O., Antronico, L., Gullà, G., 2007. Landslide triggering scenarios in homogeneous geological contexts: the area surrounding Acri (Calabria, Italy). *Geomorphology* 87, 250–267. <https://doi.org/10.1016/j.geomorph.2006.09.021>.
- Tharwat, A., 2018. Classification assessment methods. *Appl. Comput. Inform.* 17 (1), 168–192. <https://doi.org/10.1016/j.aci.2018.08.003>.
- Trigila, A., Iadanza, C., Bussetti, M., Lastoria, B., Barbano, A., 2015. Dissesto idrogeologico in Italia: pericolosità e indicatori di rischio. In: Rapporto 2015. ISPRA, Rapporti 233/2015. ISBN 978-88-448-0751-1 (in Italian). https://www.isprambiente.gov.it/files/pubblicazioni/rapporti/rapporto-233-2015/Sintesi_Rapporto_233_2015.pdf.
- van Westen, C.J., Castellanos, E., Kuriakose, S.L., 2008. Spatial data for landslide susceptibility, hazard, and vulnerability assessment: an overview. *Eng. Geol.* 102 (3–4), 112–131. <https://doi.org/10.1016/j.enggeo.2008.03.010>.
- Wasowski, J., Bovenga, F., 2015. Remote Sensing of landslide motion with emphasis on satellite multitemporal interferometry applications: an overview. In: Davies, T. (Ed.), *Landslide Hazards, Risks and Disasters*. Elsevier Inc., Amsterdam, pp. 345–403. <https://doi.org/10.1016/B978-0-12-396452-6.00011-2>.
- Winter, M.G., Wong, J.C.F., 2020. The assessment of quantitative risk to road users from debris flow. *Geoenviro. Disasters* 7 (4). <https://doi.org/10.1186/s40677-019-0140-x>.
- Winter, M.G., Shearer, B., Palmer, D., Peeling, D., Harmer, C., Sharpe, J., 2016. The economic impact of landslides and floods on the road network. *Proc. Eng.* 14, 1425–1434. <https://doi.org/10.1016/j.proeng.2016.06.168>.
- Zhang, L.M., Ng, A.M.Y., 2005. Probabilistic limiting tolerable displacements for serviceability limit state design of foundations. *Géotechnique* 55 (2), 151–161. <https://doi.org/10.1680/geot.2005.55.2.151>.
- Zhang, J., Lu, M., Zhang, L., Xue, Y., 2021. Assessing indirect economic losses of landslides along highways. *Nat. Hazards* 106, 2775–2796. <https://doi.org/10.1007/s11069-021-04566-3>.
- Zhang, Y., Ayyub, B.M., Gong, W., Tang, H., 2023. Risk assessment of roadway networks exposed to landslides in mountainous regions - a case study in Fengjie County, China. *Landslides* 20, 1419–1431. <https://doi.org/10.1007/s10346-023-02045-3>.
- Zhou, S., Huang, Y., Guo, Z., Ouyang, C., 2024. Quantitative risk assessment of road exposed to landslide: a novel framework combining numerical modeling and complex network theory. *Eng. Geol.* 343, 107794. <https://doi.org/10.1016/j.enggeo.2024.107794>.